FEUP

# ALIGNMENT OF PLANTAR PRESSURE IMAGE SEQUENCES

Pedro Nuno Silva Gomes

October 2013

Faculdade de Engenharia da Universidade do Porto


# Alignment of plantar pressure image sequences

Pedro Nuno Silva Gomes

M. Sc. Thesis
Master in Bioengineering – Biomedical Engineering

Supervisor:
Prof. Dr. João Manuel R. S. Tavares
Departamento de Engenharia Mecânica
Faculdade de Engenharia da Universidade do Porto

Porto, October 2013

# Abstract

Image registration or alignment has been widely used in several problems of computational vision. Such alignment can be described as the process of transforming an image such that correspondent areas or features are optimally overlapped between the aligned and the template images.

Plantar pressure images carry crucial information about plantar diseases and deformations and allow to infer about postural issues. Additionally, several other pathologies have been associated to the plantar pressure data as the chronic ankle instability and the diabetic peripheral neuropathy. Plantar pressure data is usually analysed by means of some parameters as the centre of pressure and the arch index.

Image registration can be extremely useful in plantar pressure images helping to reduce the number of samples needed to extract reliable parameters, to compare images acquired in different times, devices or from different patients and also allowing a more efficient diagnosis.

In this work, a principal axes (PA) based method is developed in order to address the spatial alignment of plantar pressure images. Afterwards, this method is integrated in a framework aiming to perform the alignment of image sequences both in time and space. This framework uses a dynamic programing based algorithm to match images from different sequences and then it establishes a polynomial temporal relationship between both sequences. The accuracy of the framework is accessed through the mean standard error calculation between the aligned and the template sequences. Additionally, control deformations are applied to the sequences in order to find the residual errors between original and re-aligned sequences.

The PA based method presented fast computational processing speed but poor accuracy in the spatial alignment of real images. The framework obtained better accuracy in the intra-subject spatio-temporal alignment when using high degree polynomials ($p<0.001$) up to $10^{th}$ degree.

Finally, a correlation is sought between the average of the plantar pressure parameters (extracted from the various sequences) and the parameters extracted directly from a mean sequence of images (built from the spatio-temporal aligned sequences of the same subject). High correlations were found between both variables suggesting that using only one sequence of images obtained by the mean of the spatio-temporal aligned sequences is enough to extract reliable plantar pressure parameters.

**Keywords:** plantar pressure; spatio-temporal alignment; mean sequence.

# Resumo

O alinhamento de imagem tem sido amplamente usado em vários problemas de visão computacional. Este alinhamento pode ser descrito como o processo em que uma imagem é transformada de forma a maximizar a sobreposição das áreas ou características correspondentes numa imagem modelo.

As imagens de pressão plantar podem conter informação importante acerca de doenças ou deformações plantares e podem também permitir analisar a postura. Outras patologias tais como a instabilidade crónica do tornozelo e a neuropatia diabética periférica têm sido também associadas ao estudo da pressão plantar. Alguns dos parâmetros normalmente usados para analisar a pressão plantar são o centro de pressão e o *arch index*.

O alinhamento de imagem pode ser útil quando usado em imagens de pressão plantar pois pode ajudar a reduzir o número de amostras necessárias para extrair parâmetros consistentes e para comparar imagens extraídas em diferentes momentos temporais ou por diferentes aparelhos de medição. Podem ainda permitir a comparação de imagens de diferentes pacientes e ajudar a tornar o diagnóstico mais eficiente.

Neste trabalho é desenvolvido um método de alinhamento espacial de imagens baseado no alinhamento dos eixos principais. Este método é integrado num algoritmo de alinhamento espácio-temporal. Este algoritmo usa programação dinâmica para emparelhar imagens de diferentes sequências e depois estabelece relações temporais entre as sequências através de polinómios. A precisão do algoritmo é testada através do cálculo do erro médio padrão entre as sequências alinhadas e a sequência original. São ainda aplicadas deformações espaciais e temporais conhecidas em todas as sequências com o objetivo de calcular os erros residuais entre a sequência original e a sequência realinhada. O método baseado no alinhamento de eixos principais demonstrou ser computacionalmente rápido mas pouco preciso no alinhamento de imagens reais. O algoritmo de alinhamento espácio-temporal obteve maior precisão usando polinómios de graus elevados ($p$<0.001).

Por fim, é feita a média entre os parâmetros de pressão plantar extraídos individualmente de cada sequência. Os valores obtidos foram comparados com os valores dos parâmetros diretamente calculados a partir de uma sequência média construída através das sequências alinhadas no tempo e no espaço. Foram encontradas altas correlações entre os valores obtidos pelos dois métodos, o que pode indicar que o uso de apenas uma sequência de imagens (obtida através da média das sequências alinhadas) é suficiente para extrair parâmetros de pressão plantar consistentes.

**Palavras-chave:** pressão plantar; alinhamento espácio-temporal; sequência média.

# Acknowledgments

I would like to acknowledge:

Prof. Dr. João Manuel Tavares for the supervision of the work in this Thesis as well as by his advices and support.

Francisco Oliveira, PhD in Biomedical engineering, for all support, availability and provision of all needed stuff.

My friends for the help and the advices along my academic career.

My family for all sacrifices to support and help me in this journey.

Thank you all.

# Contents

# List of figures

# List of tables

# Glossary

| | |
|---|---|
| **DPN** | Diabetic Peripheral Neuropathy |
| **CAI** | Chronic Ankle Instability |
| **PF** | Plantar Fasciitis |
| **COP** | Centre of Pressure |
| **AI** | Arch Index |
| **MAI** | Modified Arch Index |
| **CT** | Computed Tomography |
| **CTA** | Computed Tomography Angiography |
| **US** | Ultrasound |
| **PET** | Positron Emission Tomography |
| **SPECT** | Single Photon Emission Computed Tomography |
| **TPS** | Thin Plate Splines |
| **FFD** | Free Form Deformation |
| **SSD** | Sum of Squared Differences |
| **SAD** | Sum of Absolute Differences |
| **MI** | Mutual Information |
| **NMI** | Normalized Mutual Information |
| **CC** | Cross Correlation |
| **ICP** | Iterative Closest Point |
| **CPs** | Control Points |
| **MSE** | Mean Standard Error |
| **TRE** | Target Registration Error |
| **FRE** | Fiducial Registration Error |
| **FLE** | Fiducial Localization Error |
| **FEM** | Finite Elements Modelling |
| **PA** | Principal Axes |
| **XOR** | Exclusive-or |
| **RE** | Residual Errors |
| **PCC** | Pearson Correlation Coefficient |
| **ICC** | Intraclass Correlation Coefficient |

# Chapter 1 - Introduction

Image registration or alignment has been extensively used in medical image processing and analysis. The alignment is performed between a fixed and a moving image.

The temporal alignment is also possible in sequences of images. The need for image alignment arises mainly from the cases where images of the same scene are acquired from different viewpoints or times, when images are acquired by different acquisition devices and when alignment between an image of a scene and an atlas is pretended (Zitová and Flusser, 2003).

In this work, the alignment of plantar pressure images and sequences is focused. Firstly, it is convenient to understand why the alignment of plantar pressure images is important. Plantar pressure images carry crucial information about plantar diseases and deformations and allow to infer about postural issues. Additionally, several other pathologies have been associated with the plantar pressure data as the chronic ankle instability and the diabetic peripheral neuropathy.

Image registration can be extremely useful in plantar pressure images helping to reduce the number of samples needed to extract reliable parameters, to compare images acquired in different times or devices and also to compare images from different patients. Moreover it enables a more efficient diagnosis.

In this Thesis, techniques of spatial and temporal alignment of plantar pressure image sequences were developed. Using the aligned sequences (both in time and space) one hypothesis was considered: is the mean sequence of images (built from aligned sequences) equally reliable to extract plantar pressure parameters when comparing with the full set of sequences?

# 1.1 Motivation & Goals

The main idea behind this project was the development of alternative techniques to use as a pre-alignment step of a framework found in literature. Thus the main goals were:

- To understand algorithms applied to spatial and spatio-temporal alignment of plantar pressure images currently found in literature.
- To create a fast spatial alignment algorithm based in features segmentation and matching.
- To develop a fast temporal alignment algorithm to find an initial estimation of the temporal transformation values. Such procedure could be used as a pre-registration method to be integrated with a more robust subsequent step.
- To analyse both methodologies and compare results.
- To test the hypothesis that using a mean sequence of images is equally reliable than using the full dataset concerning some relevant parameters in plantar pressure studies.

# 1.2 Contributions

This Thesis contributed to increase the understanding on the problem of spatio-temporal alignment of image sequences.

Moreover it adds some knowledge and tools to the current research work in plantar pressure images:

- Principal axes method is not an accurate solution to align plantar pressure images but it would be useful to align similar images (differing only by displacements and rotation).

- Dynamic programing based algorithm is a good solution to establish matching between images from different sequences not only in plantar pressure images sequences but also in other problems.

- High degree (up to $10^{th}$ degree) polynomials can be an alternative smooth solution to describe usual temporal relations between images from different sequences.

- The developed temporal alignment framework is able to be used as a pre-alignment method in order to allow a fast convergence of an optimization method performed in a final registration step.

The final contribution of this work relies in the study of the reliability of building a mean representative sequence of images from an intrasubject dataset.

# 1.3 Structure

This Thesis follows the next structure:

**Chapter 2 – Plantar pressure data:** This chapter seeks to demonstrate the importance of plantar pressure data analysis. Some acquisition techniques are enumerated and some plantar pressure parameters with relevance in this work are described.

**Chapter 3 – Plantar pressure images registration:** In this chapter, an overview in image alignment methods is exposed. Feature and intensity based alignment methods are compared. Common steps in the alignment of images are described. Finally the works found in literature addressing plantar pressure images alignment are reviewed. A special focus is given to the studies in the origin of this work.

**Chapter 4 – Methodologies developed:** Initially, the developed spatial alignment algorithm is described. Then, the tests used to access the accuracy of this method are detailed. The second part of this chapter is the spatio-temporal alignment algorithm description. Here the spatial algorithm is not described because it is the same described before. Only temporal alignment is reported. Again tests used to measure accuracy of spatio-temporal alignment are detailed. Finally a mean sequence of images is built and compared with the original sequences by means of some relevant parameters in plantar pressure studies.

**Chapter 5 – Results and discussion:** Results from the spatial alignment are presented and discussed independently of the results of spatio-temporal alignment. In addition, the correlations between values of the parameters extracted from the mean temporal sequence and from the original sequences are accessed.

**Chapter 6 – Conclusions and future perspectives:** This chapter revises the key conclusions in this work. Starting from the developed work, some improvements and future developments are suggested.

# Chapter 2 – Plantar pressure data

## 2.1 Introduction

Plantar pressure measurements can help to understand foot dynamics and develop therapeutic footwear and orthoses for rehabilitation of some pathologies. In addition it can be an important tool in sports because studying biomechanics of walking and running helps to prevent injuries and to develop more adequate footwear and training techniques.

Concerning the plantar pressure studies, the most common pathology found in literature is the diabetic peripheral neuropathy (DPN) but other pathologies have been studied in order to find relations with plantar pressure measurements. Some of these pathologies are listed below. Moreover, some important features of acquisition devices are introduced and examples of different equipments are shown. Relevant plantar pressure parameters are further described.

## 2.2 Pathologies

- **Diabetic peripheral neuropathy (DPN)**: this pathology is a natural consequence of diabetes mellitus (DM) in most patients. DPN usually leads to foot deformities which cause increased pressure over the foot. Such increase in pressure is a main cause of foot ulceration (Waldecker, 2012). Bacarin et al. (2009) searched for a relation between plantar pressure abnormalities and the historic of ulceration in patients with DPN where ulcers were healed. This study is an example of the importance of the alignment of plantar pressure images. Image alignment can be useful when comparing images from different subjects, from the same subject collected at different times, and even from the same subject but acquired in different positions or collected by different acquisition devices.

- **Chronic ankle instability (CAI)**: this pathology is characterized by the recurrence of lateral ankle sprains. It is a common problem in athletes and responsible of a decrease in the quality of life since 32% of the subjects with a casual ankle sprain evolve to the CAI (De Ridder et al., 2012). In Morrison et al. (2010), CAI was related with a more lateral plantar pressure distribution.

- **Functional hallux limitus:** this is a common cause of the big toe pain. It can be characterized by an absence of motion of the first metatarsophalangeal joint during gait. Van Gheluwe et al. (2006) found significant relations between some plantar pressure parameters and the PF condition.

- **Plantar Fasciitis (PF):** PF is an inflammatory state of the plantar fascia. This pathology is associated with an accentuated pain in the sole of the foot. In Ribeiro et al. (2012), no relation was found between PF and the plantar pressure pattern distribution in recreational runners.

Additionally, other pathologies have been explored recently mainly by the companies developing plantar pressure measuring devices:

- **Chronic knee pain**;
- **Chronic back pain;**
- **Postural misalignments.**

Finding plantar pressure patterns and identifying potential problems helps to intervene effectively in:

- **Footwear:** one of the main industries interested in the plantar pressure devices development is the shoe industry. Nowadays orthopaedic footwear is a very common solution to alleviate pain, compensate deformations and redistribute pressure mainly in subjects with pathologies such as the nominated above.

- **Orthotics:** this a central field concerning neuromuscular and skeletal corrections. In orthotics, external devices called orthoses are developed. The lower limb orthoses are fulcral to stabilize gait, alleviate pain and correct deformities. To achieve that, the redistribution of foot pressure during gait is an important aspect.

Plantar pressure studies are extensively used to find the best orthotses configuration and in many cases to detect orthoses failures.

# 2.3 Acquisition devices

Acquisition of plantar pressure measurements is performed mainly by two types of devices: fixed platforms and in-shoe systems. All these devices are distinguished mainly by four features (Orlin and McPoil, 2000):

- **Resolution:** it is defined by the number of sensors by area since the plantar pressure measuring devices are usually constituted by an array of discrete sensors. The resolution increases with the increase in the number of sensors.

- **Sampling frequency:** this feature determines the temporal resolution of the system. Thus, the spatial frequency has to be carefully chosen according with the goal of the experiment. Obviously, if the experiment consists in analysing the plantar pressure pattern during running, the sampling frequency must be higher than in walking experiments. This feature is measured in samples by second (Hz).

- **Reliability:** this parameter is associated with the error in the measuring device. It has been suggested that collecting 3 to 5 samples is enough to increase the reliability of the measurement (Hughes et al., 1991, Gurney et al., 2008) but each device has its own specifications and needs an individual study. Additionally, walking samples are necessarily different since the subjects has no uniform walking/running patterns.

- **Calibration:** this procedure is fulcral to guarantee the validity and accuracy of the experiment data. Without calibration results may be sentenced to be meaningless.

Fixed platforms and in-shoe systems have several vantages and drawbacks. The choice for an adequate system is always taken by the physician considering the goals of the study.

1. **Fixed platforms:** the platform provides high-resolution measurements as well as a more accurate vertical force measurement (Orlin and McPoil, 2000). However, many steps are usually required which is an inconvenient in cases where the patient has a pathology as the DPN (with ulceration). Another evident problem is the alteration of the walking pattern by the patient. Commonly the patient has to perform some “walking adaptation” in the platform but there is always the possibility of an adulterated step because the patient adapts step to reach the platform. As example, two commercially available platforms are shown in Figures 2.1 and 2.2 together with some features highlighted by the manufacturing companies.

- **RSscan**

**Figure 2.1 – An example of a RSscan Footscan fixed platform (From footscanusa.com).**

**Model:**

Footscan®(1m/500Hz plate).

**Main features:**

Number of sensors (max): 4096

Sensor size: 5.08mm×7.62mm

Measurement frequency: 500 Hz

Sensor technology: resistive

Pressure range: 0 – 200 N/cm$^2$

- **Novel**

**Figure 2.2 - An example of a Novel EMED-X fixed platform (From novelusa.com).**

**Model:**

EMED® -X.

**Main features:**

Number of sensors (max): 6080

Resolution: 1 or 4 sensors/cm$^2$

Measurement frequency: 400 or 100 Hz

Sensor technology: capacitive

Pressure range: 10 – 1270 kPa

2. **In-shoe systems:** these systems are very important mainly in dynamic studies about footwear and orthotics development and surveillance. One of the main differences in relation to the fixed platforms is in the sensors. In-shoe sensors are usually less (lower spatial resolution) but they are more flexible. In spite of enabling the attachment in the shoe, such flexibility may facilitate the slip of the sensors array, compromising the accuracy of the results (Razak et al., 2012). In addition, the natural conditions of the foot as for instance the sweat can damage the sensors. As example, two commercially available in-shoe systems are shown in Figures 2.3 and 2.4.

- **Novel:**


**Figure 2.3 – Example of the Novel-Pedar –X in-shoe system (From novel.de).**

**Model:**

Pedar®-X.

**Main features:**

Number of sensors (max): 256(1024)

Scanning frequency: 20000 sensors/second

Pressure range: 15-600 or 30-1200 kPa

Sensor technology: capacitive

- **Tekscan:**

**Figure 2.4 - Example of the Tekscan F-scan in-shoe system (From tekscan.com).**

**Model:**

F-scan®.

**Main features:**

Number of sensors (max): 960

Measurement frequency: 165 Hz

Resolution: 4 sensors/$cm^2$

Pressure range: 1 – 160 psi

# 2.4 Parameters of interest

Some parameters extracted from plantar pressure images have deserved more attention in several plantar pressure studies. Olin and McPoil (2000) point peak pressure,

force and area as the main parameters in plantar pressure studies. Usually, force can be represented by the centre of pressure (COP) which is the point where the ground reaction force is applied (Roerdrink et al., 2006). Some of the parameters with interest in this work are described below.

- **Peak pressure (P):** is the maximum pressure measured in a sequence of images during a step. Supposing that *m* is the width, *n* is the height and *k* is the number of images in a sequence, *P* is given by:

$$P = max\left(P_{x,y,z}\right),\ x = 0, \dots, m\ ; y = 0, \dots, n; z = 0, \dots, k. \tag{2.1}$$

- **Centre of pressure (COP):** as said before, COP is the point of application of the ground reaction force in the time instant *t*. Usually it is represented in a 2D array where instantaneous COP positions are kept (Giacomizzi, 2011). Thus the COP trajectory during all experiment is observable in the 2D array. Basically COP coordinates are given by the weighted average (the weight is assumed by the pressure value $P_{x,y}$) of all pixels in the image. Considering that all sensors in the array have the same area, COP is found by:

$$\bar{x} = \frac{\sum_{y=0}^{n-1}\sum_{x=0}^{m-1} P_{x,y}\times x}{\sum_{y=0}^{n-1}\sum_{x=0}^{m-1} P_{x,y}}, \qquad \bar{y} = \frac{\sum_{y=0}^{n-1}\sum_{x=0}^{m-1} P_{x,y}\times y}{\sum_{y=0}^{n-1}\sum_{x=0}^{m-1} P_{x,y}} \tag{2.2}$$

The importance of COP monitoring in plantar pressure studies is well patent in the studies of Maribo et al. (2011) and Goryachev et al. (2011). Nevertheless, COP studies can be found in the most works relating pathologies and rehabilitation with plantar pressure data.

- **Arch index (AI):** the AI is a measure of the height of the medial-longitudinal arch of the foot. Cavanagh et al. (1987) developed the AI concept as the ratio of the middle area of the foot by the area of whole foot excluding toes. Thus, AI is given by:

$$\boldsymbol{AI} = \frac{\sum_{y=0}^{n-1}\sum_{x=0}^{m-1} \boldsymbol{B}_{x,y}}{\sum_{y=0}^{n-1}\sum_{x=0}^{m-1}(\boldsymbol{A}_{x,y}+ \boldsymbol{B}_{x,y}+ \boldsymbol{C}_{x,y})}, \tag{2.3}$$

where $A_{x,y}$, $B_{x,y}$ and $C_{x,y}$ are the three areas of the divided foot as shown in Figure 2.5.

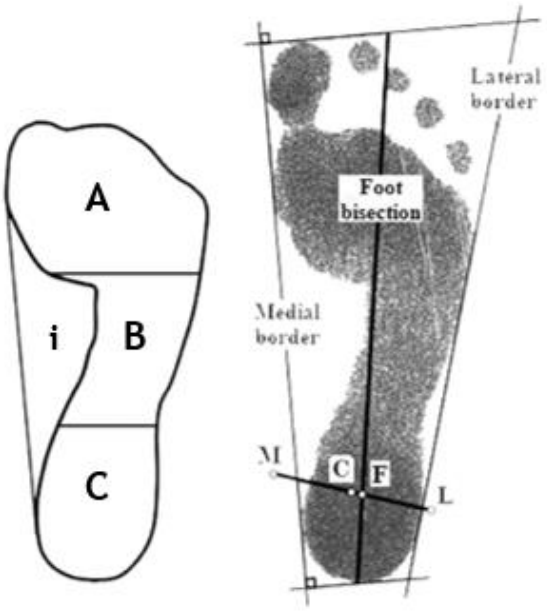


**Figure 2.5 – In the left, the division of the foot in three areas (A, B, C) and the evident exclusion of the toes. In the right, the original footprint (From Xiong et al., 2010).**

According with Roy et al. (2012), the arch of the foot can be classified as indicated in Table 2.1.

**Table 2.1 - AI classification levels. Cavus foot is the result of a high curvature whereas plan foot is consequence of the abscence of curvature.**

| | |
|---|---|
| Cavus foot | AI < 0.21 |
| Normal arch | 0.21 ≤ AI ≤ 0.26 |
| Plan foot | AI > 0.26 |

- **Modified arch index (MAI):** the MAI is found in a similar way to the AI calculation. After divide the foot in the same three regions, the sum of pressures within each area is used instead the areas. Therefore, as in Chu et al. (1995) considering the pressure in the coordinates *(x,y)* inside area A, B or C ($PA_{x,y}$, $PB_{x,y}$ and $PC_{x,y}$, respectively), the MAI is obtained by:

$$MAI = \frac{\sum_{y=0}^{n-1}\sum_{x=0}^{m-1} PB_{x,y}}{\sum_{y=0}^{n-1}\sum_{x=0}^{m-1}(PA_{x,y} + PB_{x,y} + PC_{x,y})} \tag{2.4}$$

MAI has been quite used in clinical studies. An example may be found in Nakhaee et al. (2008) where MAI is calculated in order to find relationships between sports injuries

and the height of the medial longitudinal arch. In this study there is no strong correlation between both variables.

## 2.5 Summary

Plantar pressure measurements have been carried out in several studies related with gait and various pathologies as the diabetic peripheral neuropathy which has been strongly related with plantar pressure patterns change. The study of plantar pressure images has allowed to prevent or heal foot ulceration. Chronicle ankle instability, functional hallux limitus, plantar fasciitis, chronic knee pain, chronic back pain and postural misalignments are examples of other pathologies related with plantar pressure investigation.

The importance of plantar pressure studies is well remarked in the development of orthopaedic and sports shoes as well as the orthoses. These special shoes and orthoses can alleviate the pain and correct deformations in the patients.

There are two types of plantar pressure acquisition devices: in-shoe-systems and fixed-platforms. The main technical features distinguishing such devices are the resolution, sampling frequency, reliability and calibration.

There are important parameters giving quantitative and qualitative information about the plantar pressure pattern. In this study, peak of pressure, centre of pressure, arch index and modified arch index are used.

Frequently, the researcher is dealing with too much information to analyse and large variations (mainly between foot positions) in the different trials. It is important to simplify and maximize the information acquired in plantar pressure measurements in order to help the diagnosis/study of plantar pressure related pathologies. Thus, in this work, strategies are developed to accomplish these needs.

# Chapter 3 – Plantar pressure images registration

## 3.1 Introduction

Nowadays, medical imaging is probably one of the most valuable tools in the medical diagnosis, surgery planning and evaluation. Several imaging techniques are available in the medical area, and a patient often performs more than one image exam to monitor or detect health problems. These exams may be from the same modality or from different modalities. Some of the most common are: X-ray, computed tomography (CT), computed tomography angiography (CTA), magnetic resonance imaging (MRI), magnetic resonance angiography (MRA), ultrasound (US), single-photon emission computed tomography (SPECT) and positron emission tomography (PET).

Sometimes, the image analysis is very difficult to the physician and it depends greatly on his experience to mentally combine (or merge) data from different images or volumes. Many computational methods have been used in order to provide more efficient visualization and analysis of medical images like image segmentation, filtering, features enhancement, registration, fusion, etc. Image registration is an important tool because it allows finding common shapes and structures between images and establish spatial/temporal correspondences that facilitate complex tasks of image analysis.

Image registration is commonly referred as the process of aligning two images or even temporal sequences of images on a common spatial/temporal coordinate system. In this work, the image/sequence used as template to perform registration is always designated as “fixed image/sequence” whereas the image/sequence to be aligned is called “moving image/sequence”.

Some of the most important applications of image registration helping medical diagnosis are the combination (fusion) of data from images of same modality or different modalities; the search for differences in size and shape over a time range; the application on image-guided surgery and the comparison between the image from a patient and an image database or atlas (Hajnal et al., 2001).

The advantages of using image registration in clinical environment are evident. Instead of using avoidable images, the data provided can be combined in a minimum dataset containing only the relevant information exploited at a maximum point. Subsequently, the time per patient and overall monetary costs are decreased to the clinic. In addition, patients may be protected from excessive radiation exposure (by means of the reduction in the multiple imaging exams).

In recent years, image registration has gained importance in plantar pressure images analysis. The alignment of such images is a difficult task because plantar pressure images are acquired with different step frequencies and foot positions since every person has a different gait and even the same person may have different gait along the time (see chapter 2). Consequently, an image from a sequence may not correspond to the image with the same index in another sequence. Additionally, the shape of the object and the intensities of the pixels vary in an unpredictable manner between images from different sequences. Thus, the registration may be useful finding spatial/temporal correspondences between steps from the same individual or different individuals and integrating their data in a meaningful way facilitating visualization.

Frequently, the researchers are dealing with an important trade-off: the accuracy of the alignment against the processing time. In the particular case of the plantar pressure images, the accuracy is very important, but a real time processing would also be highly desirable for using in clinical applications (e.g. physiotherapy).

# 3.2 Image registration techniques

## 3.2.1 - Classification

Registration methods may be divided according to different criteria. Maintz and Viergever (1998) suggested a classification based on nine subdivided criterions. Later, this classification was reduced to eight categories by Fitzpatrick et al. (2000). Those criterions are dimensionality, registration basis, geometrical transformation, domain of transformation, degree of interaction, optimization procedure, modalities, subject and object. A brief description of each criterion is presented below:

- Dimensionality: usually medical images are in three-dimensional (3D) space, but sometimes they are bi-dimensional (2D). Additionally, it is possible to consider time as

a dimension in temporal sequences of images. Most common registration methods are classified as 2D/2D, 2D/3D, 3D/3D and 4D/4D.

- Registration basis: this criterion considers the nature of the features used in the registration procedure. These features may be intrinsic or extrinsic relatively to the patient data. Extrinsic features are added to the patient facilitating their visualization by any imaging modality. As result, registration of acquired images is faster and less complex (Maintz and Viergever, 1998). Extrinsic features may be invasive or non-invasive (less accurate). In turn, intrinsic methods use only patient internal data as landmarks (anatomical or geometrical characteristics extracted from images), segmented structures (e.g. points, curves, surfaces) or features obtained from voxel properties.

- Geometrical transformation: classification of registration techniques can also be made according with the mathematical model used to map points from an image to another. If lines are mapped onto lines, a projective transformation is occurring; when parallel lines are mapped onto parallel lines, it is considered affine transformation; if only rotations and translations are allowed (dimensions and angles are unaltered), it is called rigid transformation, and if lines are mapped to curves, an elastic or curved transformation is used.

- The domain of the transformation is classified as global if all image data is used and local if only particular image features are used.

- Degree of interaction: the registration algorithm may be automatic, semi-automatic or interactive relatively to the user interaction. Ideally, the automatic procedure is preferable and many researchers have been developing automatic algorithms. Sometimes human interaction is desired because speed and accuracy may be increased.

- Optimization procedure: the parameters used in the transformation can be found by direct computing or by maximizing or minimizing a function to iteratively find the optimum.

- Modalities: registration can be achieved in monomodal (images from the same modality), multimodal (images from different modalities), modality to model (registration is performed between an image and a model) or patient to modality (registration is performed between an image and the patient himself) applications.

- Subject: images may be from the same patient (intrasubject), from different patients (intersubject) or from a patient and a database built from many patients (usually referred as atlas).

- Object: categorization is also made according with the anatomic region involved in the registration procedure. Head (Ashburner, 2007; Christensen et al., 1994, Shen, 2007; Studholme et al., 1996) and pelvis (Shen, 2007) are some examples frequently found in literature.

## 3.2.2 – Feature vs. Intensity based methods

The main difference between feature and intensity based methods is the segmentation step in which relevant correspondent features are extracted from images. Thus, the first step in feature based methods is image segmentation.

Image segmentation techniques are used to extract points or sets of points (pixels) with a particular interest from an image. Such points may be part of contours, lines, regions within an intensity range, etc. Image segmentation techniques have been widely used in medical images. Usually, these techniques are used to find features exposing pathologies in the images. Nevertheless, segmentation has been also used in image registration because finding correspondent features in different images allows to calculate a geometrical transformation to use in the matching of those images. In this case, a common approach to obtain easily identifiable features to facilitate segmentation is to use a stereotactic frame screwed to the skull of a patient or markers glued to the skin. However, such approach is obsolete and several new features segmentation techniques have been used helping image registration procedure. As example of segmentation relevance in image registration, in McLaughlin et al. (2002) blood vessels were skeletonized in 2D digital subtraction angiographies and in a 3D model of phase contrast magnetic resonance angiographies in order to establish matching and register 2D images with the 3D model.

One possible approach to match those features is to define a cost matrix containing the distances or costs of each possible matching and then find the matching which minimizes the global cost. Based on this optimal matching, the geometric transformation between both images can be found by the least squares technique per example (Oliveira et al., 2009a).

Intensity based methods do not use a segmentation step. Instead a similarity measure based in the intensity values of the images is optimized in an iterative procedure. Usually, in each iteration the geometric transformation is changed according with the optimization technique and then it is applied to the moving image. Thus, the new moving image is mapped to the new coordinates and the similarity measure is calculated. The objective is to minimize or maximize that similarity measure. Several different interpolation methods are used to resample the new image.

An alternative solution can be the use of a hybrid method. These methods usually consist in a pre-registration procedure using a feature-based method followed by the improvement of the obtained geometric transformation by an intensity based method.

Another important difference between both techniques is the processing time. Usually, intensity based methods are more accurate but computationally heavy due the optimization algorithm. In turn, feature based methods are frequently fast but less accurate. It is important to evaluate the trade-off between pretended speed vs. accuracy in the choice of the method.

## 3.2.3 – Geometrical transformation

The choice for the geometrical transformation between images is very important. Basically, the geometrical transformation is a mapping function that maps the pixel coordinates from a "moving" image to a "fixed" image. The accuracy and the computational processing time of the registration algorithm depend crucially on the choice of the geometrical transformation. After this choice, the estimation of the mapping function is performed in order to find the most suitable values. In 1D, this mapping function may be conceptually described as:

$$T: x \mapsto x' \Leftrightarrow x' = T(x) \tag{3.1}$$

where *T* is the mapping function mapping ***x*** to ***x'***.

Some of the most common mapping functions in 2D space are presented below (an overview is depicted in Figure 3.1).

Converting the pixel 2D coordinates to homogeneous coordinates, a transformation matrix can be used to represent the projective transformation and its subsets (affine, similarity and rigid).

The projective transformation is useful to relate 3D anatomy with 2D images acquired from a patient (Fitzpatrick, 2000). Its representation in 2D space is given by:

$$\begin{bmatrix} x' \\ y' \\ w \end{bmatrix} = \begin{bmatrix} a_{11} & a_{12} & t_x \\ a_{21} & a_{22} & t_y \\ b_1 & b_2 & 1 \end{bmatrix} \begin{bmatrix} x \\ y \\ 1 \end{bmatrix} \tag{3.2}$$

where parameters $a_{11}$, $a_{12}$, $a_{21}$ and $a_{22}$ are representing deformations, $t_x$ and $t_y$ are representing translations, $b_1$ and $b_2$ give the projection point, $w$ is a dependent parameter used to normalize pixel coordinates.

In this approach, rotation, scale, shear, translation and perspective projection (conferred by non-zero values of $b_1$ and $b_2$) are transformed. The straightness of lines is kept. At least, four corresponding points are needed in both images.

Affine transform is frequently applied to global models in which the transformation is valid to all image area, and can be represented in 2D as:

$$\begin{bmatrix} x' \\ y' \\ w \end{bmatrix} = \begin{bmatrix} a_{11} & a_{12} & t_x \\ a_{21} & a_{22} & t_y \\ 0 & 0 & 1 \end{bmatrix} \begin{bmatrix} x \\ y \\ 1 \end{bmatrix} \tag{3.3}$$

In Equation 3.3, $b_1$ and $b_2$ (from Equation 3.2) are set to 0 (zero).

This transformation keeps straightness of lines and their parallelism, but it may change the angles between them (Fitzpatrick, 2000). In this transformation, a minimum of three non-collinear corresponding points are needed between both images.

The similarity transform is a sub-case of affine transform. Usually, it is applied globally. Considering rotation angle as $\theta$, similarity transform can be represented in 2D space as:

$$\begin{bmatrix} x' \\ y' \\ w \end{bmatrix} = \begin{bmatrix} s.cos(\theta) & -s.sin(\theta) & t_x \\ s.sin(\theta) & s.cos(\theta) & t_y \\ 0 & 0 & 1 \end{bmatrix} \begin{bmatrix} x \\ y \\ 1 \end{bmatrix} \tag{3.4}$$

This transform only performs scaling, rotation and translation. Thus, angles and curvatures are preserved. This mapping function needs a minimum of two control points from both images (Zitová and Flusser, 2003). As obvious, if more corresponding points are used, the accuracy can be raised and the computing time can be reduced.

The rigid transform (also known as Euclidian transform) is a subset of the similarity transform. In 2D space, it is defined as:

$$\begin{bmatrix} x' \\ y' \\ w \end{bmatrix} = \begin{bmatrix} cos(\theta) & -sin(\theta) & t_x \\ sin(\theta) & cos(\theta) & t_y \\ 0 & 0 & 1 \end{bmatrix} \begin{bmatrix} x \\ y \\ 1 \end{bmatrix} \tag{3.5}$$

In this approach, angles between lines, length between points and areas are held; only rotation and translations occur. This transformation is computed from a minimum of two corresponding points in both images. Rigid transform is preferentially used in registration of rigid structures and in the pre-registration step as initial approximation (Oliveira and Tavares, 2012a).

The curved transformations are frequently used in medical images registration (Oliveira and Tavares, 2012a). In fact, it is reasonable to say that this transformation, also known as elastic or deformable, is more adequate for most studies related with medical images because non-rigid deformations in almost all structures of the body are possible. Some of the most used curved transformations in the last years have been based on splines. Generally, in splines-based methods, after finding the corresponding points from both images (the fixed and the moving images) a spline is used to establish correspondences.

Spline-based methods may interpolate or approximate the displacement of the corresponding points allowing to map their locations in the target image.

Some of the most popular splines are the thin plate splines (Rohr et al., 2001) and the B(asis)-splines (Mattes et al., 2003; Oliveira and Tavares, 2012b; Rueckert et al., 1999).

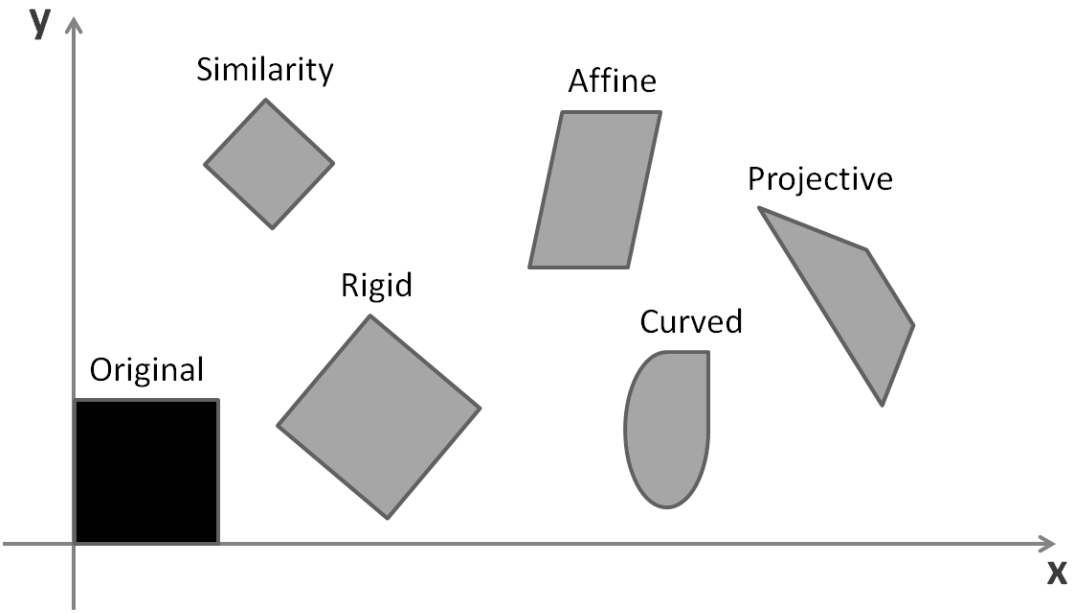


**Figure 3.1 - Representation of 2D geometric transformations applied to an "Original" square.**

Thin plate splines (TPS) is a global transformation, because if a corresponding point is changed, all other points are also changed (Crum et al., 2004; Oliveira and Tavares, 2012). It belongs to the radial basis functions family. Thus, B-splines based transformations may be considered as local transformations. B-Splines are from the free-form deformation (FFD) class since they deform an object by changing a mesh of control points. The number of degrees of freedom and the consequent computational cost are highly dependent of the control points mesh dimensions (Rueckert et al., 1999). Another common approach are the polynomial functions of a degree higher than one (Oliveira and Tavares, 2012a).

## 3.2.4 – Similarity measures

**Figure 3.1 - Representation of 2D geometric transformations applied to an "Original" square**

Similarity measures assess how much two images overlap. There are similarity measures more suitable for intensity-based registration methods, more appropriate for feature-based registration methods or even for both classes of registration methods.

A similarity measure based on pixel intensity differences is the sum of squared differences (*SSD*) or the normalized sum of squared differences that is given by:

$$SSD = \frac{1}{N}\sum_{x=0}^{N-1}[A(x) - B\big(T(x)\big)]^2 \tag{3.6}$$

where *N* is the number of pixels of all the image, or just from a region of interest of the image, *A(x)* is the intensity of image *A* in position *x* and *B(T(x))* is the intensity of corresponding point in image *B* estimated by the transformation *T(x)*. This similarity measure is commonly used in intensity-based methods and assumes that the corresponding points should have similar intensities (Oliveira and Tavares, 2012a). This assumption has a drawback: *SSD* measure is very sensitive to the Gaussian noise, i.e. to pixels with large intensity differences. The optimum is achieved to the minimum value of *SSD*. As this method assumes approximate intensity values between the same structures, it is only adequate for monomodal registration. In order to minimize the sensitivity to the Gaussian noise, the sum of absolute differences (*SAD*) may be used:

$$SAD = \frac{1}{N}\sum_{x=0}^{N-1}[A(x) - B\big(T(x)\big)] \tag{3.7}$$

In a study of Hoh et al. (1999), SAD is compared against another similarity measure, the stochastic sign change – SSC, applied in the rigid registration of PET images.

Another similarity measure widely used in intensity-based registration methods is the cross-correlation (CC):

$$CC = \frac{\sum_{x=0}^{N-1}(A(x)-\bar{A}).(B\big(T(x)\big)-\bar{B})}{\sqrt{\sum_{x=0}^{N-1}(A(x)-\bar{A})^2.\sum_{x=0}^{N-1}(B\big(T(x)\big)-\bar{B})^2}} \tag{3.8}$$

where *N*, *A(x)* and *B(T(x))* are the same parameters defined for *SSD*, and $\bar{A}$ and $\bar{B}$ are the mean of all intensities in the pixels of image *A* and *B*, respectively. In this approach, corresponding pixels have a linear intensity relationship; as such, it is more adequate for monomodal registration. A high cross-correlation is desirable with the aim of finding the optimum.

Mutual information (*MI*) has been an extensively used similarity measure in the last years. It is based in information theory and reveals how much information an image contains about a second one (Oliveira and Tavares, 2012a; Rueckert et al., 1999). This measure considers probabilistic relationships between intensities, and its value is obtained from the entropies of the intensity distribution:

$$MI = H_A + H_B - H_{AB} \tag{3.9}$$

where $H_A$ and $H_B$ represent the Shannon's entropy of the pixels in image *A* and *B*, respectively, and $H_{AB}$ represents their joint entropy, which is achieved by a joint histogram. These entropies are obtained by:

$$H_A = -\sum_{i=0}^{N-1} P_i log P_i \tag{3.10}$$

$$H_B = -\sum_{j=0}^{N-1} P_j log P_j \tag{3.11}$$

$$H_{AB} = -\sum_{i=0}^{N-1} \sum_{j=0}^{N-1} P_{ij} log P_{ij} \tag{3.12}$$

where $P_i$ and $P_j$ are the probability of intensity *i* to appear in target image and the probability of intensity *j* to appear in moving image, respectively. $P_{ij}$ is the joint probability of both intensities occurring at the same position. The MI has a maximum if the images are correctly aligned.

The normalized mutual information (*NMI*) model was developed to minimize the overlap problem of *MI* (Studholme et al., 1999):

$$NMI = \frac{H_A + H_B}{H_{AB}} \tag{3.13}$$

Unlikely *SSD* and *CC*, MI-based methods are proper for multimodality registration since there are no direct relations between intensities. *MI* may also be used in monomodality registration.

## 3.2.5 – Optimization

The optimization procedure changes the parameters from the transformation model in order to maximize/minimize the similarity measure. This is an iterative approach where the initial transformation is gradually improved until there is no possibility to obtain a better value to the similarity measure. One of the greatest challenges in image registration is to avoid local optimums because optimization algorithms may converge to non-global optimums which lead to poor registration results. A common approach to minimize this problem is the multiresolution scheme. In this scheme, images are registered at low resolution and the transformation obtained is used as starting approach for a next registration at higher resolution. This is a hierarchical approach. In order to obtain the low resolution images, a low-pass filter can be used to smooth large peaks of intensity. Thus, the multiresolution scheme allows a faster convergence, and it decreases the probability of converging to local optimums.

One of the most used optimization methods is the iterative closest point (*ICP*) (Besl and McKay, 1992). This method is useful in matching optimization since matching and geometric transformation can be simultaneously sought in feature-based methods (Oliveira and Tavares, 2012a). Matching is a needed step in feature-based methods in order to establish correspondences between features extracted from the images to be registered. Therefore, these features are aligned in image registration procedure. *ICP* is an algorithm which iteratively searches for the minimum distance between pairs of control points. Usually, transformation parameters are estimated iteratively until a stopping criterion. As a conceptual example, it can be considered a surface with a set of points $p_j$ and a model surface $X$ in another image. *ICP* algorithm iteratively searches for the minimum value of:

$$d(p_j, X) = \min(\left|\left|x - p_j\right|\right|) \tag{3.14}$$

where $d$ is the distance between $p_j$ and the closest point x in the model surface.

Other optimization methods used to maximize or minimize a similarity measure have been intensively explored in the last years. Some of these methods are Powell's Method, Downhill Simplex Method, Steepest Gradient Descent and the Conjugate Gradient Method. These methods are well detailed in Press et al. (2007).

## 3.2.6 – Interpolation

The interpolation process arises from the necessity of finding new intensity values of pixels when they are mapped to new positions by a transformation. Frequently, nearest neighbour or bilinear interpolation are satisfactory methods. However, more accurate methods may be necessary. Usually, there is a convolution between the image and an interpolator kernel. Some of the other interpolator kernels are: quadratic splines, cubic B-Splines, Gaussians and truncated *sinc* functions (because *sinc* functions have infinite extent). The nearest neighbour interpolator basically assigns the nearest pixel intensity value to the pixel being interpolated. Frequently, the nearest neighbour interpolator is avoided because of the high probability of artefacts occurrence in the resultant image. The choice for an adequate method is highly dependent of the desired trade-off between accuracy and computational cost. A review of some interpolation methods is performed in Thévenaz et al. (2000), and in Lehmann et al. (1999) several interpolation methods are compared.

## 3.2.7 – Accuracy evaluation

Image registration methodologies need to be evaluated according with their accuracy. Typically, accuracy is not easy to assess because errors may be hidden during the registration process or even undistinguishable from natural differences of the input images. There are three typical errors which can affect final result: localization error (due to

inaccurate detection of control points (CPs) [corresponding features]); matching error (resulting from false matches in correspondences found between CPs) and alignment error (due to wrong choices in transformation model or its parameters). Obviously, the simplest approach to evaluate the accuracy is the visual evaluation by an expert. The mean square error (***MSE***), a statistical measure, may be applied to the CPs to assess the alignment error between them. Another method consists on using target registration error (***TRE***) which is the displacement between a pair of CPs after registration. TRE is given by:

$$TRE = a - T(b) \tag{3.15}$$

where *a* is a point from image *A* and *T(b)* is the corresponding point in image *B* after transformation. Those points should have some anatomical significance.

Fiducial registration error (***FRE***) is another possible measure for registration errors. Fiducial points are reliable corresponding point pairs for registration purposes. In order to determine fiducial points within a distinct feature (fiducial feature), a fiducial localization is needed. The error resulting from incorrect fiducial localization is known as fiducial localization error (***FLE***). The fiducial registration error (***FRE***) quantifies the misalignment caused by ***FLE*** when fiducial points are aligned in the registration process. ***FRE*** is given by:

$$FRE = a_i - T(b_i) \tag{3.16}$$

where $a_i$ is a point from the fiducial feature *i* in image *A* and $T(b_i)$ is the corresponding point from the same fiducial feature in image B after transformation.

The difference between ***FRE*** and ***TRE*** is that in ***TRE*** corresponding points with clinical or anatomical relevance are used, while ***FRE*** uses corresponding points from easily visible structures that can have clinical interest or not. The clinical relevance of ***TRE*** is an advantage of this measure. Both ***TRE*** and ***FRE*** are applied only in rigid registration methodologies (Fitzpatrick et al., 1998). Frequently, ***FRE*** is also represented as a root mean square of the distance between corresponding points:

$$FRE = \frac{\sqrt{\sum_{i=1}^{N}[a_i - T(b_i)]^2 {w_i}^2}}{N} \tag{3.17}$$

where $N$ is the total number of fiducial features and $w_i$ is an optional weighting factor used to give different influence to each fiducial feature $i$ in the total measurement of *FRE*. The weighting factor is useful because fiducial features may not be equally reliable.

Another approach is to compare the results from an image registration method under evaluation against a gold-standard method. If no gold-standard method exists, the comparison has to be made with a different method and if the results are similar there is high probability of high accuracy (it is a qualitative measure). A consistency test is also used and consists on the assumption that rigid registration from image A to B produces the same results when the same transformation model is applied from B to A (Crum et al., 2004).

# 3.3 Plantar pressure images and sequences alignment

## 3.3.1 – Spatial Alignment

Harrisson and Hillard (2000) and Tavares et al. (2000) accomplished the first studies in plantar pressure images registration. In the first, images are aligned by the principal axis method whereas in Tavares et al. (2000), the plantar pressure images are matched using finite elements modelling (FEM) techniques applied together with a modal matching method. Later, modal matching and FEM methods were also used in plantar pressure images in the works of Bastos and Tavares (2004) and Pinho and Tavares (2004).

In Pataky et al. (2008b), seven different rigid-body methods for intrasubject plantar pressure image registration are compared. In this study, it was found that manual registration can be an acceptable solution when averaged across raters since no significant difference was found between this method and the global methods optimizing a similarity measure (*MSE*, Probability-weighted variance, mutual information (*MI*) and exclusive-or (*XOR*)). In addition, the principal axes (*PA*) method was the faster method but achieved poorer results than the previously referred methods.

An improvement in plantar pressure images registration was accomplished in the work of Oliveira et al. (2009a). This work presents a feature based method where feet contours are segmented and then points from these contours are matched through a dynamic programming based algorithm (Figure 3.2). The main contribution of this work was the high decrease in the computational speed of the algorithm since there was just a small increase in mean-*MSE* values comparing with the best results of the previous work of Pataky et al.

(2008b). In Oliveira et al. (2009b) only points from contours with high affinity are considered in order to avoid wrong matches between points without correspondence.

In Oliveira et al. (2010), pedobarographic images are registered using phase correlation and cross correlation methods in the frequency domain. The major claim in this work is the improvement of accuracy and robustness comparing with the results of the contour based method presented in Oliveira et al. (2009a, 2009b). In addition, the low processing time is preserved. Another vantage of this algorithm is the robustness in the presence of Gaussian noise.

In Oliveira and Tavares (2012c), five different registration methodologies are compared in terms of accuracy, robustness and computational speed. The alignment based in the contours matching was the fastest but achieved the worst accuracy whereas the best accuracy was obtained for the algorithms using the optimization of a similarity measure based in Powell's method. Considering that this optimization was performed after a pre-registration step, in addition to the higher accuracy, the algorithm also showed low processing time since the geometric transformation estimated in the pre-registration step was very close to the optimal solution.

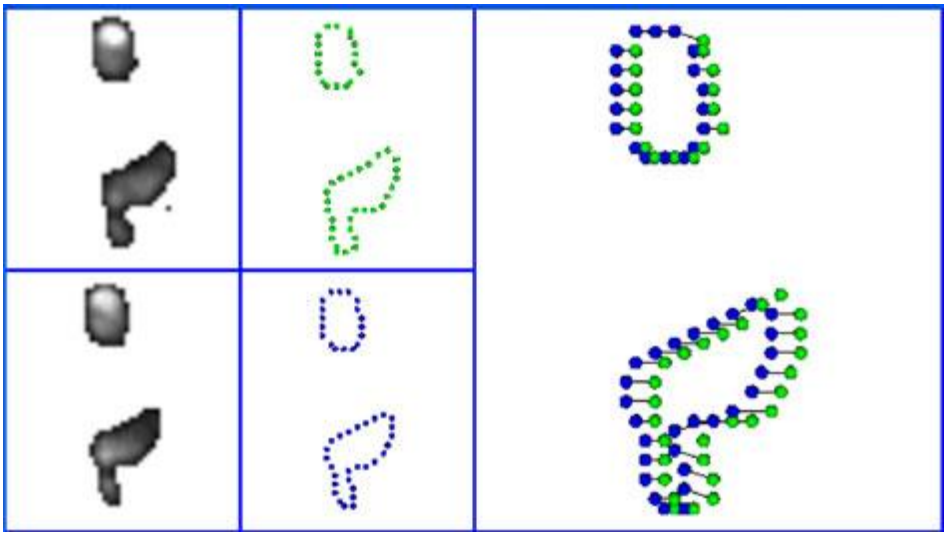

**Figure 3.2 – In the left are the fixed and moving image. In the middle the extracted contours are shown. The right image represents the matching between the contours. (From Oliveira et al., (2009a)).**

In Oliveira et al. (2012d), the importance of plantar pressure images alignment is very pronounced. In this work, an automatic foot classification algorithm is developed (Figure 3.3). The alignment of the images is performed by the cross-correlation algorithm of Oliveira et al. (2010). The automatic classification algorithm allows to distinguish images of the left and the right foot. Additionally, arch index and modified arch index are automatically measured and no significant difference is found between these automatic measurements results and the traditional measurements results. This algorithm also showed high robustness to data from different sources (EMED and Footscan systems).

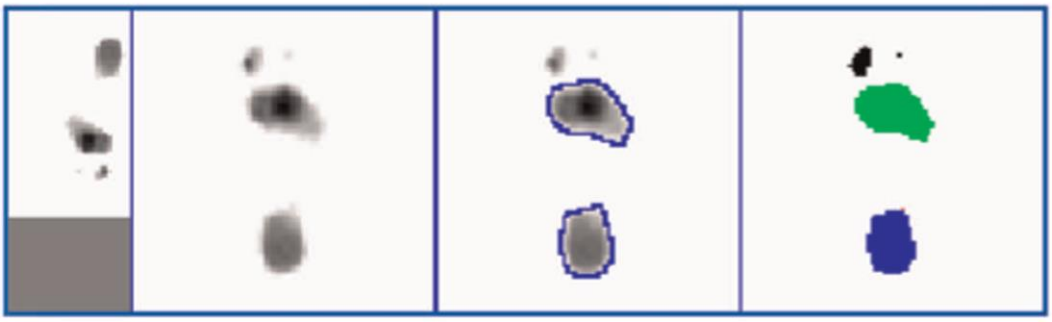

**Figure 3.3 – Algorithm developed in Oliveira et al. (2012d) to calculate AI and MAI. In the left is the original image. In the second square the image was rescaled, aligned and the pressure was normalised. In the third square the toes are removed and in the last square, the foot (without toes) is divided into different foot regions. (From Oliveira et al. (2012d)).**

## 3.3.2 – Spatio-temporal Alignment

More recently, the temporal alignment of plantar pressure image sequences has been studied. The pioneering study of Oliveira et al. (2011b) showed the advantages of the spatio-temporal alignment. In this work, the spatial alignment is performed by using the cross-correlation maximization method followed by an optimization of a similarity measure. In turn the temporal alignment was performed concurrently by using polynomial functions up to 4th degree. The temporal alignment algorithm has a pre-alignment stage and an optimization stage. In the pre-alignment stage, a linear relationship is established between images indexes from both sequences considering that the first and last images from the fixed sequence correspond to the first and last images of the moving sequence. Then, the optimization is performed simultaneously with the spatial optimization by the Powell's based method with line optimization by Brent's method.

In addition, the temporal optimization scheme used two approaches: one where first and last images of fixed sequence must correspond to the first and last images of the moving sequence ("constrained" optimization) and another where there are no dependences between parameters ("unconstrained" optimization). The main findings were the better results obtained by $2^{nd}$, $3^{rd}$ and $4^{th}$ degree comparing with the linear temporal transformation when aligning real images sequences. In addition, the constrained optimization produced worst results comparing with unconstrained optimization.

In a more recent study (Oliveira and Tavares, 2012b), B-Splines were used instead of polynomials. B-Splines showed better accuracy than polynomial functions referred in previous work.

# 3.4 Summary

Image registration or alignment has been an important tool helping in medical image analysis and processing. There are two common procedures used in image alignment: feature based methods and intensity based methods. Usually, the first step in feature based methods is the image segmentation. Such procedure allows to extract important common features from "fixed" and "moving" images. These features are then matched and a geometrical transformation (found through established matching) is employed in the moving image. In turn, the intensity based methods use a similarity measure between image pixels intensities and then optimizes iteratively the values of the geometrical transformation between both images. A common approach is to use a combination of a feature based method with an intensity based method in an approach known by "hybrid registration". The image resampling is often performed by an interpolation kernel which is chosen according with the accuracy/computational processing speed trade-off.

Any developed alignment methodology should be validated. This requirement is achieved using an accuracy measurement technique. Two possible solutions used to measure the accuracy of the alignment are the calculation of a similarity measure value or the fiducial registration error.

Plantar pressure images alignment has been extensively developed. Such investigation started with the works of Harrisson and Hillard (2000) and Tavares et al. (2000). Meanwhile, relevant studies in plantar pressure images alignment were realized. A contour matching based method was used in Oliveira et al. (2009b) and a Fourier based method was proposed in Oliveira et al. (2010) in order to align peak pressure images. Recently, the temporal alignment of plantar pressure image sequences was also proposed in Oliveira et al. (2011b) and Oliveira and Tavares (2012b). In Chapter 4, an alternative solution to the spatio-temporal alignment of plantar pressure image sequences is presented. Additionally, the reliability of using such methodology to build a mean sequence of images is also accessed by a procedure described in Chapter 4.

# Chapter 4 – Methodologies developed

## 4.1 Introduction

In this work, the spatio-temporal alignment of plantar pressure image sequences was addressed. The study was divided in two parts: firstly, the spatial alignment is studied alone aiming to find the accuracy and processing speed of just the spatial alignment independently of the temporal alignment. In the second part, the accuracy and processing speed for the developed spatio-temporal algorithm were assessed. The algorithm for the spatio-temporal alignment has three steps: firstly the spatial alignment is made between the peak pressure images built from the fixed and moving sequences, then the temporal alignment is done between those sequences and finally, the spatial alignment is refined by a new optimization of the rigid transformation values.

In all experiments the first step was the establishment of a region of interest (ROI). ROI is defined as the minimum area containing plantar pressure data in both peak pressure images. ROI is important to increase computational speed since unnecessary calculations are avoided.

Whenever possible, data used in other studies were used to allow comparisons.

The implementation of all algorithms was performed in C++ using Microsoft Visual Studio 10 in a PC notebook with an Intel® Core™2 Duo CPU T7250 2GHz processor, 3GB of RAM and running Windows 7.

Dataset and all steps of spatial and spatio-temporal alignment are described in detail in this chapter.

The accuracy was statistically accessed by Statistical Package for Social Sciences (SPSS) 21.0 using two-sided t-tests.

# 4.2 Dataset

All image sequences used in this work are the same used in Oliveira et al. (2011b) and Oliveira and Tavares (2012b). So, a total of 156 image sequences were used. These images were collected from 26 individuals. Each individual performed 6 trials (3 for each foot) in order to increase the reliability of samples since a minimum of three to five measurements are advised in plantar pressure measurements (Hughes et al., 1991).

By image sequence, it should be understood a sequence of images acquired during a step of an individual. All sequences were acquired at a frequency rate of 25 frames per second using an EMED system (AT model from Novel, Germany). Other main features of this device are the pressure sensibility of 5 kPa, the resolution of 2 sensors/$cm^2$ and a pressure range between 10 and 1270 kPa.

Individuals were 7 men and 19 women. Men had mean age of 18.4±0.5 years old, weight of 68.6±6 kg and height of 1.73±0.07 m. In turn, women had mean age of 20.4±2.3 years old, weight of 58.3±6.3 kg and height of 1.64±0.05 m. The individuals were selected according with no history of relevant deformities or disabilities affecting gait. In order to increase the comfort with the experimental devices and procedures, the individuals walked over the plantar pressure measuring device several times. Further details about acquisition procedure can be found in Oliveira and Tavares (2012b) and Oliveira et al. (2011b).

# 4.3 Spatial registration

## 4.3.1 – Peak pressure image building

In order to perform spatial registration of image sequences, a representative image from each one is built. It is assumed that the subject has a uniform step meaning that there is no displacements or rotations between foot images in the same step. That fact makes sense because typically from the moment that someone places the heel on the platform, foot follows a uniform direction over the full step.

Then, assuming a usual step, each representative image must have relevant information about each pixel over the full set of images. Maximum intensity is the parameter used to achieve that requirement. Thus, each resultant image contains the maximum pressure measured at each pixel along the entire sequence. Representing a sequence of images by $T(x, y, i)$, and a peak pressure image by $PP(x,y)$, one has:

$$PP(x,y) = \max\big(T(x,y,i)\big), i = 0, \dots, size - 1 \tag{4.1}$$

where (*x*,*y*) are the pixel coordinates, *i* is the temporal coordinate of the sequence and *size* is the number of images in the sequence.

Spatial registration is performed using the resultant images. Other image features can be used to obtain representative images from sequences such as the mean over each pixel. However, there are many studies using peak pressure images (Oliveira and Tavares, 2012b, 2012c; Oliveira et al., 2011b). This fact is very important since it allows comparing results knowing that there is no influence of representative image calculation methodology.

## 4.3.2 – Principal axis registration

The principal axis method has been widely used in spatial alignment of 2D images. This method does not require to find correspondences between images. Instead, it can find the angle and displacements in both images using directly features of image or whole the input data.

Here, the first step is centroids calculation. Considering a peak pressure image *PP(x,y)* with height *n* and width *m*, centroids are given by:

$$\bar{x} = \frac{\sum_{y=0}^{n-1}\sum_{x=0}^{m-1} PP(x,y)\times x}{\sum_{y=0}^{n-1}\sum_{x=0}^{m-1} PP(x,y)}, \qquad \bar{y} = \frac{\sum_{y=0}^{n-1}\sum_{x=0}^{m-1} PP(x,y)\times y}{\sum_{y=0}^{n-1}\sum_{x=0}^{m-1} PP(x,y)} \tag{4.2}$$

Aiming to find angles between principal axes, eigenvectors of peak pressure images are calculated. Thus, finding eigenvectors requires eigenvalue decomposition of the covariance matrix (*C*):

$$C = \begin{bmatrix} PP_{xx} & PP_{xy} \\ PP_{yx} & PP_{yy} \end{bmatrix} \tag{4.3}$$

where:

$$PP_{xx} = \frac{\sum_{y=0}^{n-1}\sum_{x=0}^{m-1} PP(x,y)\times(x-\bar{x})^2}{\sum_{y=0}^{n-1}\sum_{x=0}^{m-1} PP(x,y)} \tag{4.4}$$

$$PP_{xy} = \frac{\sum_{y=0}^{n-1}\sum_{x=0}^{m-1} PP(x,y)\times (x-\bar{x})\times (y-\bar{y})}{\sum_{y=0}^{n-1}\sum_{x=0}^{m-1} PP(x,y)} \tag{4.5}$$

$$PP_{yy} = \frac{\sum_{y=0}^{n-1}\sum_{x=0}^{m-1} PP(x,y)\times(y-\bar{y})^2}{\sum_{y=0}^{n-1}\sum_{x=0}^{m-1} PP(x,y)} \quad (4.6)$$

and $PP_{yx} = PP_{xy}$.

Hence, considering the square matrix $C$, its eigenvalues are the roots calculated from the characteristic equation (4.7). Knowing that $C$ is a 2×2 matrix, there are 2 roots in the characteristic equation meaning 2 eigenvalues. So, to each eigenvalue there is an associated eigenvector. Letting the eigenvalues be represented by $\lambda$ and the identity matrix by $I$, the characteristic equation comes:

$$\det(A - \lambda I) = 0 \quad (4.7)$$

Assuming that $(A - \lambda I)$ is singular, there is a non – zero solution to:

$$(A - \lambda I)\, x = 0 \quad (4.8)$$

so that $x$ is the eigenvector of $A$. Simplifying eq.4.8:

$$\mathrm{A}\, x = \lambda x \quad (4.9)$$

Should be noted that $x$ gives only the vector direction and not the magnitude. To the current purposes in this work, such information is enough.

Finally, the angle between principal axes of both peak pressure images is calculated using the inner product of vectors $x_1$ and $x_2$:

$$\theta = \cos^{-1}\left(\frac{x_1.x_2}{\|x_1\|\|x_2\|}\right) \quad (4.10)$$

Translation in $x$-axis and $y$-axis of the moving image in relation to the fixed image is calculated by the difference between them centroids after rotate moving image in $\theta$ radians.

After getting the angle and translations between images, a rigid transformation is applied to the moving image because only intra-subject alignments are performed. Additionally, shape deformations were not desired.

## 4.3.4 – Optimization method

The optimization method employed in spatial alignment is the same used in Oliveira et al. (2011b) and Oliveira and Tavares (2012b). Thus, a brief description is done here. The full description of the algorithm can be found in Press et al. (2007).

The algorithm used here is based on Powell's method with line optimization by Brent's method.

The concept of Powell's method employed in this work can be briefly described by Figure 4.1.

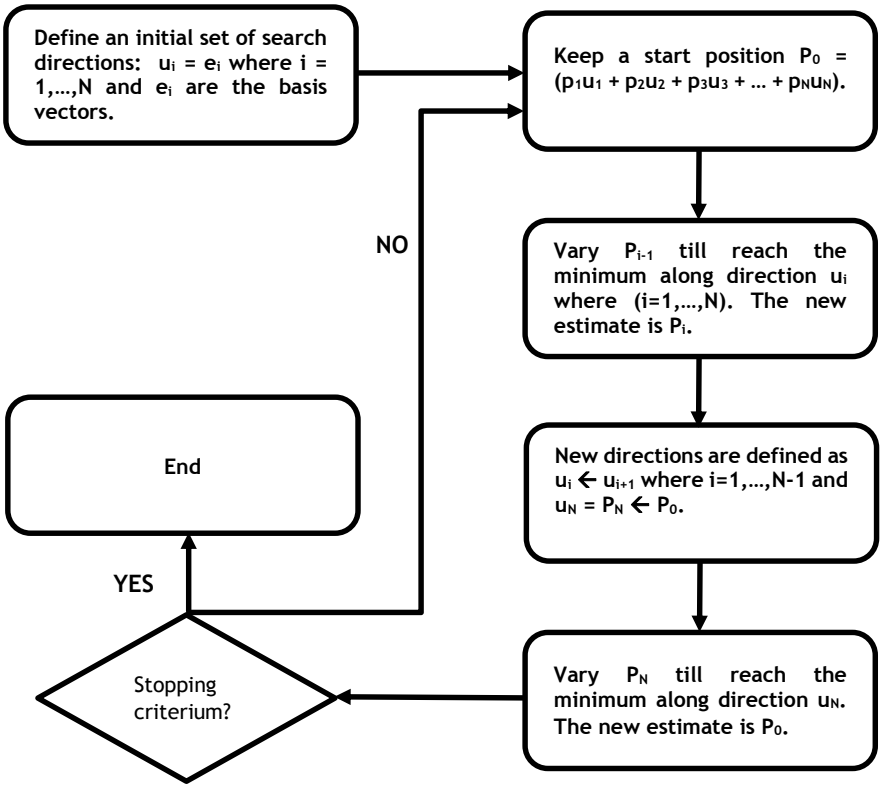


**Figure 4.1 – Flowchart representing the behavior of Powell's based alghorithm.**

## 4.3.5 – Accuracy assessment

## 4.3.5.1 – Using MSE between images

Considering that each individual performed three trials for each foot, there are three peak pressure images (one by sequence) by foot. Thus, two alignment procedures are performed by each foot from each individual giving a total of 112 alignments.

*MSE* is used as a measure of accuracy between the peak pressure images in each alignment. After the spatial alignment, *MSE* is calculated between the aligned (moving) image and the fixed image. As stated before, the smaller the *MSE* value, the better the spatial alignment. Notice that this *MSE* measure is calculated only in the pixels with non – zero values in order to allow comparisons with works from other authors.

*MSE* values are calculated for three distinct alignment procedures:

- Using principal axis method considering different intensities in centroids calculation (real image);

- Using principal axis method but considering a binary image in centroids calculation, i.e., pixels intensity greater than zero were equalized to one whereas the remaining pixels remain zero;

- Using principal axis method (considering binary intensities) to perform pre-registration and then refining the found transformation values through optimization based in Powell's method combined with Brent's line optimization method. The similarity measure minimized in this optimization is the *MSE* (over all pixels of the image). Additionally, image resampling during optimization procedure is performed by bi-linear interpolation.

## 4.3.5.2 – Using control deformations

A known deformation is applied to all 156 peak pressure images. This deformation is used as a gold-standard deformation since after the alignment between original image and deformed image, both are compared by means of the residual errors (RE). RE is calculated as:

$$RE = \sum_{y=0}^{N-1} \sum_{x=0}^{M-1} \left( \sqrt{(T(x) - T'(x))^2 + (T(y) - T'(y))^2} \right) \quad (4.11)$$

where *T* is the known control transformation and *T'* is the transformation found by the alignment procedure. Basically, *RE* is the sum of squared differences between pixels positions mapped by *T* and estimated by *T'*.

As in Oliveira and Tavares (2011), the control deformation is designed using the values of Table 4.1. Unfortunately, reliable comparisons between the results of both works are not allowed since datasets are quite different.

**Table 4.1 – Spatial control deformation parameters.**

| | |
|---|---|
| Rotation angle (α) | 12° |
| Translation in x-axis ($T_x$) | 2.5 pixels |
| Translation in y-axis ($T_y$) | -3.2 pixels |

Again, RE values are calculated for the alignment using principal axis method considering real pixel intensities, considering binary intensities and also the alignment using the principal axis method (using binary intensities) as pre-alignment tool and a final improvement with the optimization based on Powell's method.

# 4.4 Spatio - temporal registration

## 4.4.1 – Sequence expansion

In order to perform a better matching between images from different sequences, the moving sequence is "expanded" by trilinear interpolation. This expansion allows to obtain a higher sampling frequency. In the experimental dataset used, the standard frequency of acquisition (*f*) was 25 images per second giving a period (*T*) of 40ms between two images, so the number of images per second is posteriorly increased by a multiplication factor *m*:

$$f = \frac{m}{T} \tag{4.12}$$

Additionally, if the first image of the moving sequence (M) has the best match with the second or higher image of the fixed sequence (F) (Figure 4.2) means that a frame with data temporarily before the initial frame in the moving sequence is needed.

For this purpose, an initial set of frames is linearly extrapolated in the sequence. Notice also that an equal number of images is linearly extrapolated at the end of the sequence by the same reason.

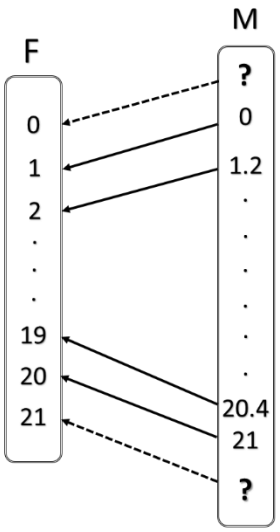


**Figure 4.2 – Representation of a hypothetical problem when images are not extrapolated before the first image and after the last images. In this case, the matching algorithm gives a worst global matching because it forces a wrong match between the first and last images of both sequences.**

As inferred through Table 4.2, if a moving sequence has 20 frames, the expanded sequence would have (20 × *m*) + m frames. Sequence expansion is an important step because the best matching between images is made, the better the curve (described by a polynomial function) fits data.

**Table 4.2 - Example of sequence expansion using *m*=3. If the original sequence has 3 images, the new (expanded) sequence would have 3 × 3 + 3 = 12 images.**

| Original sequence index | Expanded sequence index |
|---|---|
| - | $-1$ |
| - | $-\,{}^{2}/_{3}$ |
| - | $-\,{}^{1}/_{3}$ |
| 0 | 0 |
| - | ${}^{1}/_{3}$ |
| - | ${}^{2}/_{3}$ |
| 1 | 1 |
| - | $1+\,{}^{1}/_{3}$ |
| - | $1+\,{}^{2}/_{3}$ |
| 2 | 2 |
| - | $2+\,{}^{1}/_{3}$ |
| - | $2+\,{}^{2}/_{3}$ |

## 4.4.2 – Cost matrix

Matching between images from different sequences has to be performed taking into account a parameter quantifying similarities between features or intensities of images from both sequences. Here, the main interest is to maximize/minimize the total matching cost depending of the used measure. So, assuming a moving sequence *M* and a fixed sequence *F*, a cost matrix is designed containing the individual costs to match each image of *M* with each image of *F*. If the aim is to minimize the total matching cost value, in the end of the matching process, the sum of the individual costs is minimal. The individual matching cost is represented by $c_{ij}$ along this work.

In a first approach, the Euclidian distance between the images centroids (from different sequences) was used as measure of individual cost. However, MSE was used lately instead. MSE was preferred over the Euclidean distance between centroids because results were much better. Thus, each cell of cost matrix has a value given by eq. 4.13, where *N* and *M* are width and height of the images respectively, considering that all images have the same size.

$$MSE_{ij} = \frac{1}{N \times M} \sum_{x}^{N} \sum_{y}^{M} [F(x, y, i) - M(x, y, j)]^2 \tag{4.13}$$

By each cost matrix corresponding to the matching between sequences, *MSE* is calculated $i \times j$ times ($i$ is the total number of images in sequence *F* whereas $j$ is the total number of images in sequence *M*).

## 4.4.3 – Dynamic programming

Matching between images from different sequences is performed by an algorithm based on dynamic programming developed and described by Oliveira et al. (2009b) and Oliveira and Tavares (2008).

Originally, that algorithm was developed to align contours preserving their absolute and relative orders. Main advantages of this algorithm comparing with common used algorithms like Hungarian Method are the low processing time and the avoidance of cross matches. An example of contours matching using this algorithm is depicted in Figure 4.3.

If a contour is defined by points {0, 1, 2, 3, 4, 5, 6, 7, 8}, the sequence {8, 0, 1, 2, 3, 4, 5, 6, 7} is the same contour. Thus, in the first case, the points of the sequence are

monotonously increasing. Adopting the definition of Oliveira and Tavares (2008), it is said that the first sequence preserves absolute order. The second sequence does not preserve the absolute order but only the relative order.

In this work, the algorithm is applied only to monotonous increasing sequences (the step images are always increasing in time). By this reason the concept of relative order is not meaningful here and the algorithm was modified in order to avoid unnecessary calculations. Indexes from two different images sequences can be viewed as two distinct "opened contours" where the circular matching is impossible. After finding the cost matrix this algorithm minimizes the global cost given by the sum of individual matching costs.

**Figure 4.3 – Matching between two different contours with different number of points using the algorithm of dynamic programming (From Oliveira and Tavares, 2008).**

Consider the indexes of two hypothetical image sequences *T* and *S*:

$$T = \{0, 1, 2, 3, 4, 5, 6, 7, 8\},$$

$$S = \{0, 1, 2, 3, 4, 5, 6, 7, 8, 9, 10\}.$$

If the two sequences have the same number of images, then the first image of sequence *T* has necessarily to correspond to the first image of sequence *S*, the second to the second and so on. However, if the size of both sequences is different, more matching possibilities are allowed.

Knowing that the absolute order has to be kept, index 0 of sequence *T* can be matched with index 0, 1 or 2 of *S*. If index 0 of *T* is matched with index 1 of sequence S, then index 1 of *T* can only be matched with index 2 or 3 from sequence *S*. In order to know

the number of images of *S* available to be matched with an image of *T*, the state variable *s* is used. Thus between *T* and *S* there are three matching hypothesis, *s* = 3.

Oliveira and Tavares (2008) defined a function $f_k(s)$ used to find the minimum cost of matching points 0,1,…,*k* of a sequence when each image has *s* matching possibilities. Thus, for each *k* the function $f_k(s)$ is calculated *s* times.

The main steps of the algorithm are shown in Figure 4.4. Considering sequences *T* and *S*, a table with 9 columns (k=9) and 3 rows (*s* = 11-9+1) is built. Values of $f_k(s)$ are calculated as in Table 4.3.

In the example of Table 4.3, starting by the cell in (*9*, *3*) position, a reverse search is performed in order to find the matching of minimum global cost. Firstly, the cell corresponding to the state containing the minimum value is chosen in the last column, then the same procedure is done to the next columns. If the minimum value is in the second row, in the next column only the values of first row and second row are compared. Supposing that cell in position (8, 2) is selected, a matching between images 7 of sequence *T* and 8 of sequence *S* is established.

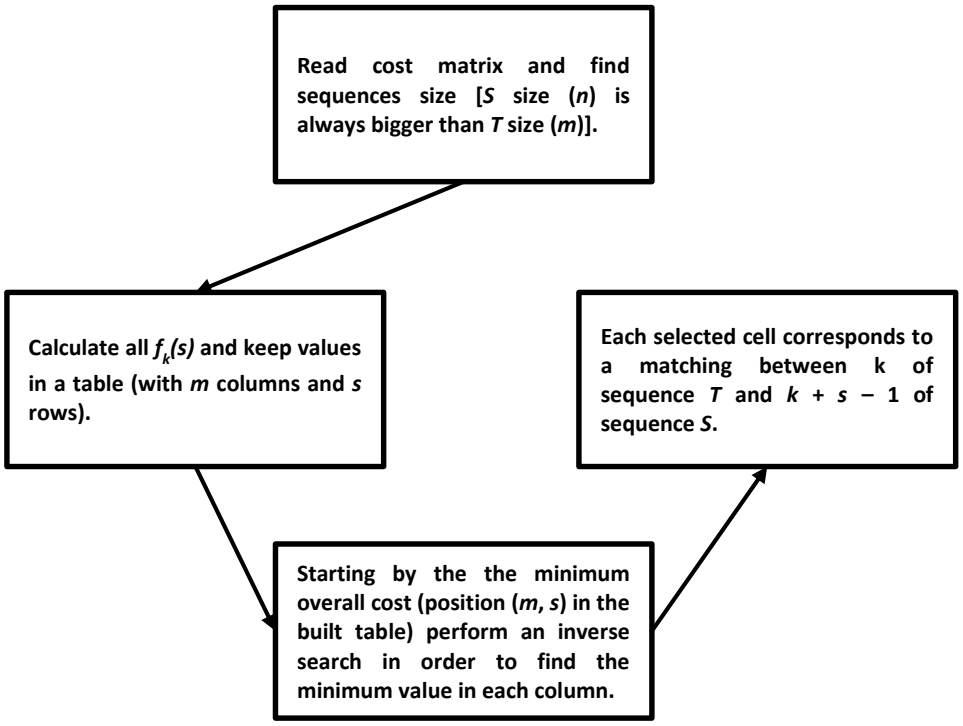


**Figure 4.4 – Sequential steps of the dynamic programming algorithm.**

**Table 4.3 – Example of $f_k(s)$ calculation for the sequences *T* and *S*.**

| | | | |
|---|---|---|---|
| $f_1(1) = c_{11}$ | $f_2(1) = c_{22} + f_1(1)$ | ……. | … |
| $f1(2) =$ minimum$\{c_{11}, c_{12}\}$ | $f_2(2) =$ minimum$\{f_2(1), c_{23} + f_1(2)\}$ | | … |
| $f_1(3) =$ minimum$\{c_{11}, c_{12}, c_{13}\}$ | $f_2(3) =$ minimum$\{f_2(1), f_2(2), c_{24} + f_1(3)\}$ | | $f_9(3) =$ minimum$\{f_9(1), f_9(2), c_{9,11} + f_8(3)\}$ |

## 4.4.4 – Curve fitting

After establishing correspondences by dynamic programming, a polynomial was employed to create a mathematical relationship between images indexes from both sequences. Polynomial coefficients were estimated by the least squares technique.

Thus, polynomials of different degrees were used in order to approximate a curve passing near all points previously found. Polynomials have the advantage of enabling to create a "smooth" curve, avoiding high time steps between images data (data gaps) and sometimes minimizing the adverse effect of less correct matches.

The degree of the polynomial has to be chosen carefully because high order polynomials are more prone to instability (Figure 4.5).

The most important condition concerning the polynomials usability in temporal alignment is that the index *i*+1 must be higher than *i* for both sequences. This means that inflection points are not desirable at all in the polynomial curve because time is never decreasing. Consequently, the curve has to be a strictly increasing function.

After finding polynomial coefficients by the least squares technique, images of the new sequence are interpolated. Thus, to each image of the fixed sequence, a new image of the moving sequence is interpolated.

The new index *i'* of the moving sequence is estimated by the polynomial which can be generically represented as:

$$i' = c_0 + c_1 i + c_2 i^2 + c_3 i^3 + c_4 i^4 + c_5 i^5 + \cdots + c_n i^n \quad (4.14)$$

where *n* is the polynomial degree, $c_1$, $c_2$, …, $c_n$ are the coefficients found previously, *i* is the index of an image in the fixed sequence and *i'* is the index of a new image (in the moving sequence) to interpolate.

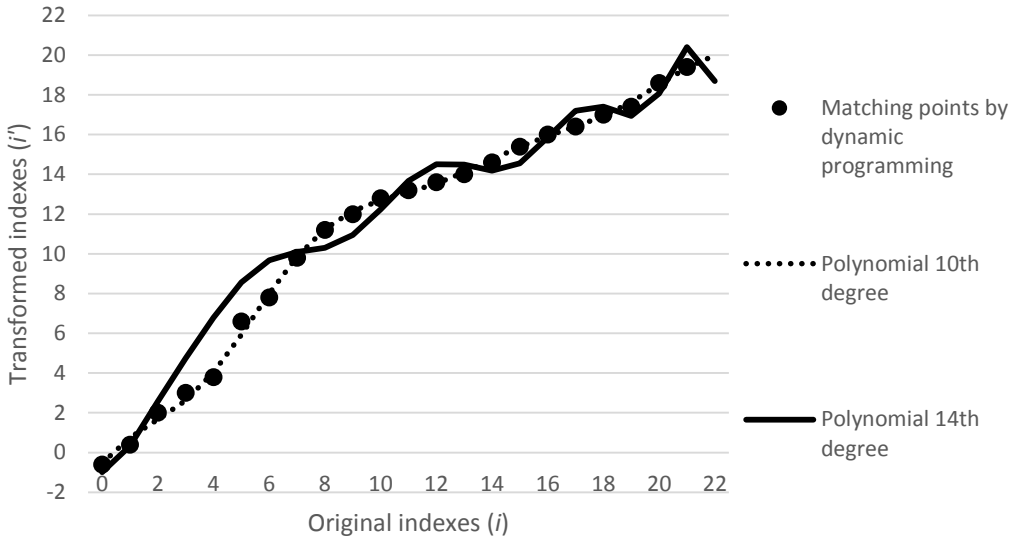


**Figure 4.5 – Comparison between two different high degree polynomials when fitting the set of found matchings. Whereas 10th degree polynomial fits well the matched points the 14th degree polynomial shows instability.**

Polynomials up to 10th degree are tested. From this degree, curve instability is observed (example in Figure 4.5).

## 4.4.5 – Accuracy assessment

Two different solutions are used in order to compare accuracy of the alignment as in Oliveira et al. (2011b) and Oliveira and Tavares (2012b). These methods were chosen to allow comparisons with the results of both works.

## 4.4.5.1 – Using MSE between image sequences

MSE over non – zero pixels is used as a measure of accuracy between real sequences of images. Thus, after the spatio-temporal alignment of the moving sequence, MSE is calculated as described before between the aligned (moving) sequence and the fixed sequence. It should be remarked that the smaller the MSE value, the better the spatio-temporal alignment.

Polynomials between 4th and 10th degree are used to align all sequences. Additionally, for each degree, the moving sequence is previously expanded by a multiplication factor between 2 and 8. Thus, MSE is calculated 7 (degrees) × 112 (alignments) × 7 (m factor) giving a total of 5488 times.

### 4.4.5.2 – Using Control deformations

Two known temporal deformations are applied to all the 156 sequences, aiming to allow comparisons with Oliveira and Tavares (2012b). The temporal control deformations used are presented in Table 4.4.

**Table 4.4 – Temporal control deformations used. *i* represents the image index in original sequence whereas *i'* represents the image index in deformed sequence.**

| | |
|---|---|
| Linear | $i' = 1.15i$ |
| Curved | $i' = 0.9i + 2\sin(i + 3)$ |

Additionally, a rotation of -15° is applied to all image sequences by a rigid transformation in order to spatially deform sequences.

After aligning sequences, the obtained and the control transformations are compared by means of the residual errors. Results are given as mean temporal error and mean spatial error which are the average of the differences between image indexes and pixel positions, respectively.

## 4.5 Plantar pressure parameters extraction

### 4.5.1 – Overview

One of the objectives of this work was to show the influence of the spatio-temporal alignment in common plantar pressure parameters. In the Thesis of Tábuas (2012) the following findings are pointed:

- The parameters extracted from a mean image (calculated from the peak pressure images which are built from the spatially aligned sequences) are strongly correlated with the average of the parameters directly extracted from each peak pressure image (without alignment).

- The choice for the fixed image in the alignment method does not influence significantly the values of the extracted parameters.

Here, instead of a mean peak pressure image, a mean sequence of images is created. Then the peak pressure image is extracted from this representative sequence. In addition, not only the spatial alignment is employed but also the temporal alignment.

The plantar pressure related parameters considered in this work are the COP, the peak of pressure, the AI and MAI. All values are found by the framework proposed by Oliveira et al. (2012d).

COP is calculated in relation to the foot axis and the foot limit. The foot axis is determined as in Chu et al. (1995) and the posterior limit is given by the position of the closest point to the inferior limit of the image (Figure 4.6). Thus, a longitudinal axis is defined perpendicularly to the foot axis (red) and passing through the found point. Then, COP position relatively to the foot axis is calculated. This variable is negative if is located in the medial part of the foot (relatively to the foot axis). Previous assumptions are also valid to the maximum pressure pixel calculation. COP coordinates are obtained by the Equation 2.2 and maximum pressure pixel is found by Equation 2.1.

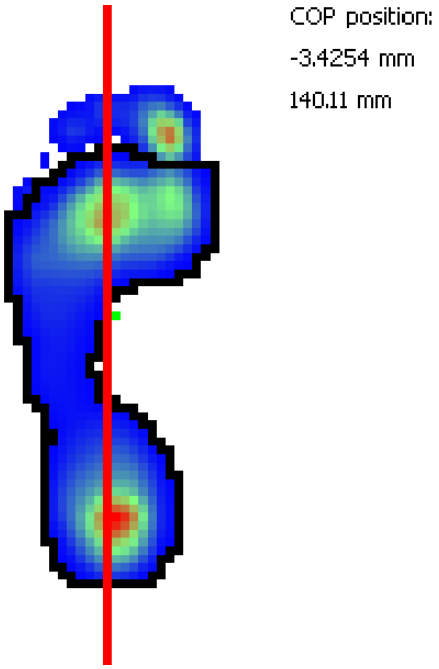


**Figure 4.6 – Representation of COP values calculation. The red line is the foot axis and the green point outside the foot is the COP position. As COP is located in a medial position relatively to the foot axis, its value is negative. (Computed using the framework presented in Oliveira et al.(2012d)).**

With the purpose of finding AI and MI values, some image processing is needed. Firstly, the input image is rescaled and centred to acquire similar dimensions to a template image. The next step is the spatial alignment of this last image with the template image. After pixels pressure normalisation, the foot is classified as left or right. Afterwards the toes are removed from the image and the foot is divided in three areas. In addition, the foot

length is calculated. When the classified foot is divided in the three areas AI and MAI are calculated by equations (2.3) and (2.4), respectively. As pointed before, such procedure is performed by the framework presented in Oliveira et al. (2012d) and it is generically illustrated in Figure 3.3.

## 4.5.2 – Dataset

In order to compare a set of image sequences with a mean sequence, two stages are followed:

**A.** Parameters are extracted directly from each sequence. Then, the average between parameters of the same foot from the same individual is calculated. Notice that the left and right foot are compared independently.

**B.** All sequences are aligned by the spatio-temporal framework described in this work. The first sequence of each foot is used as fixed sequence to the alignment. The spatial alignment is performed using the PA method to estimate initial values for a rigid geometric transformation. Then these values are optimized by the framework described in Chapter 4.3.4.The temporal alignment uses the 10$^{th}$ degree polynomial with $m$ = 5. Linear interpolation is the preferred resampling method.

Then, a mean sequence (*meanSeq*) of $n$ aligned sequences of images ($G_1$, $G_2$, …, $G_n$) is built:

$$meanSeq(x,y,z) = \frac{\sum_{z=0}^{z=k-1}\sum_{y=0}^{y=j-1}\sum_{x=0}^{x=i-1}[G_1(x,y,z)+ G_2(x,y,z)+\cdots+ G_n(x,y,z)]}{n} \quad (4.15)$$

Finally, a peak pressure image is calculated from *meanSeq* and the pretended parameters are found in this image.

The average and the standard deviation of all parameters were computed using *Microsoft Excel 2013*.

Pearson correlation coefficient (PCC) and Intraclass correlation coefficient (ICC) were assessed between results obtained by the approaches *A* and *B*.

The PCC measures the linear dependence between two different variables. The PCC values can be classified as in Table 4.5.

**Table 4.5 – Classification of PCC values.**

| | |
|---|---|
| PCC ≤ 0.25 | Poor correlation |
| 0.25 < PCC ≤ 0.50 | Reasonable correlation |
| 0.50 < PCC ≤ 0.75 | Good correlation |
| PCC > 0.75 | High correlation |
| PCC = 1 | Total correlation |

In turn, ICC quantifies the consistency between measurements of the same quantity. ICC is generically classified as in Table 4.6.

**Table 4.6 – Classification of ICC values.**

| | |
|---|---|
| ICC < 0.4 | Poor reliability |
| 0.4 ≤ ICC < 0.75 | Reasonable reliability |
| ICC ≥ 0.75 | High reliability |

Pearson correlation coefficient and the Intraclass correlation coefficient were computed using *Statistical Package for the Social Sciences (SPSS) 21.0*.

# 4.6 Summary

Principal axes based methods are used in this work aiming to perform spatial alignment between peak pressure images (built from each sequence). Considering a rigid geometrical transformation between both images, the rotation angle is calculated between the principal axes of the objects and the translations are calculated by the differences between the centroids of the fixed and rotated images. Three different methods are employed: principal axes method over real pixels, principal axes over binary pixels and principal axes over binary pixels followed by an optimization procedure. The accuracy is accessed by MSE calculation in real images alignment and RE calculation in the alignment of deformed images (by a known rigid transformation) with the original images.

In the spatio-temporal alignment, the first step is the spatial alignment of peak pressure images using the principal axis method followed by the optimization framework. Then, a cost matrix is built quantifying the MSE between different frames of both sequences. A matching algorithm based on dynamic programming is used in order to establish the

matching of minimum global cost and finally polynomials of different degrees are used to establish a relationship between images of both sequences. The polynomial coefficients are found by the least squares technique. Previously, the number of images in the input sequences is increased in order to achieve a better matching and avoid polynomial instability. Finally, the spatial transformation is refined by a new optimization step.

The accuracy is accessed by the MSE calculation in the real image sequences alignment. In addition, linear and curved temporal deformations together with a spatial rotation are applied in all image sequences. The mean spatial and temporal errors are calculated between original and aligned sequences after the deformation.

Mean images (average between images with the same index) are built from the aligned sequences resulting in a mean sequence. Peak pressure pixel, COP, AI and MAI are calculated for the mean sequence and also for each original sequence (in this case, the mean of these parameters is performed for each foot of each individual). Then, intraclass correlation coefficient and Pearson correlation coefficient are accessed between parameters values found by both methods.

In Chapter 5, results of the described methodologies are presented and discussed.

# Chapter 5 – Results and discussion

## 5.1 Spatial alignment

### 5.1.1 – MSE assessment

Results of the spatial alignment with the three used methods are shown in Figure 5.1. Here, the accuracy is given by the mean MSE values over all the aligned peak pressure images extracted from all real dataset sequences. As shown, the principal axis method considering real pixel intensities achieved the worst results by far. In turn, when binary pixels intensity are considered, mean *MSE* suffered a large drop to approximately half of the value obtained by the previous referred way. Moreover, the optimization procedure was employed to refine the results obtained by the *PA* method (over binary pixel intensities) and a large drop of mean *MSE* value relatively to the other two procedures was evident again.

Large variations between mean *MSE* results from the three employed methods are evidencing the weaknesses of *PA* method when deformations between images are not purely rigid. Starting with an analysis of the *PA* method using real pixels intensity, it is clear that the principal axis and centroids calculations were not accurate. Even thinking that the alignments were only performed in feet from the same subject, feet has not necessarily the same pressure distribution and the same shape when contact with the pressure measuring device in each step. Thus, thinking that centroids and principal axis calculations have a total geometrically dependence, it is logic to conclude that these parameters were highly affected by the geometrical differences between steps images. Theoretically, *PA* method would have better results the more geometrically similar were the steps. Even if this method is not accurate can be satisfactory to perform a pre-alignment step mainly if objects have large rotations or translations and have only small shape deformations. Such hypothesis was crucial to choose this method and to apply it in this work since the main goal was to obtain a fast pre-alignment spatial technique.

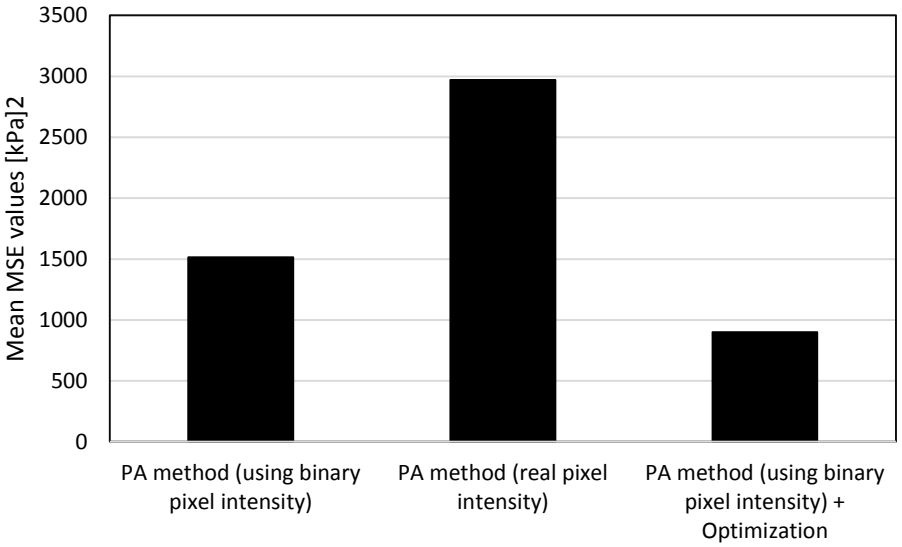


**Figure 5.1 – Mean MSE values (over non-zero pixels) computed for the spatial alignments using real images. Three different methods were used and the results compared.**

Using a binary image in PA method, only the geometrical shape of the object influences centroids and PA calculations. This detail explains the high difference relatively to the mean MSE using real intensity values. In the last, besides the geometry, also different intensity distribution over the image influences the results. However, considering only binary images, only geometry differs. It was shown that between steps the main difference affecting PA method accuracy is surely the pressure distribution over the foot images. Nevertheless, the optimization framework showed that the *PA* method using a binary image is still far from the optimal results despite allowing the convergence of the optimization algorithm to an optimal solution.

## 5.1.2 – RE assessment

The mean and maximum RE values were calculated for all peak pressure images built from image sequences and deformed by a known rigid transformation. Therefore, the three alignment procedures were used to find that transformation and align the images. *RE* values for the alignment of the deformed images are shown in Table 5.1 together with the processing time. The smallest mean *RE* value between both *PA* methods was achieved using the real intensities values. This finding is not in accordance with the previous one where using real images resulted in higher mean *MSE* values and consequently the worst result. When the deformation between images is purely rigid without geometric or data differences, PA method is a good solution. The difference in *RE* results between both *PA* methods

(without optimization) can be explained by the image resampling because linear interpolation may change slightly geometric shape.

Real intensities are used as a weighting factor because the higher the intensities of the pixels the more influence that pixels have in centroids and *PA* calculations. Thus, using real intensities, it is minimized the influence of the geometry in cases where intensities distribution is similar for both images.

**Table 5.1 – Mean and maximum RE values computed for the alignment of a deformed image (by a known rigid deformation) with the original image. Computational processing speed of the algorithm is also presented. Three different alignment methods are compared.**

| Spatial alignment method | Mean RE ( pixels) | Maximum RE ( pixels) | Speed (ms) |
|---|---|---|---|
| PA method (binary images) | 0.404 | 1.188 | 4.795 |
| PA method (real images) | 0.003 | 0.038 | 4.709 |
| PA method (binary images) + Optimization | 1.73e-07 | 2.12e-05 | 1330.235 |

From Table 5.1 is also evident a large drop in *RE* values when using the optimization framework. Although such drop has an adverse effect in the processing time, since many iterations are needed to achieve this large drop in *RE* values.

Processing time is about 5ms using just the *PA* methods. Using optimization this time rises nearly 400 times (about 1.3 seconds). Here, there is a trade-off between accuracy and speed. Knowing that 0.003 pixels corresponds approximately to 0.021mm, it is reasonable to consider that the mean *RE* result (obtained to the *PA* method using real intensities) is a good result because it is much lower than the resolution of the pressure measuring device. In the case of the alignment of real sequences of plantar pressure images, the optimization algorithm seems to be very important due to the weakness of *PA* method in presence of variations in geometry and intensity distribution. Nevertheless, in this case where images only differ by a rigid deformation, *PA* method using real intensities can be enough to produce accurate results. However, using only the *PA* method over binary images could not be a good solution because the maximum *RE* was approximately 8.4 mm which is bigger than the spatial resolution of the device.

# 5.2 Spatio - temporal alignment

## 5.2.1 – MSE assessment

In order to compare different order polynomials performance in real sequences temporal alignment, the mean *MSE* values were calculated and the results found are shown in Table 5.2. Moreover, by each degree mean *MSE* values were calculated for different multiplication factors (*m*). Notice again that the fixed sequence has always *m*=2. Before the temporal alignment, the spatial alignment was performed using the *PA* method over the peak pressure binary images and then the optimization framework was employed. By Table 5.2, one can confirm that the drop in the mean *MSE* values is patent when the degree is increased for almost all *m*.

**Table 5.2 – Mean MSE values computed for the spatio-temporal alignment of real image sequences using different degrees and multiplication factors (*m*).**

| | Multiplication factor (m) | | | | | | |
|---|---|---|---|---|---|---|---|
| Degree | 2 | 3 | 4 | 5 | 6 | 7 | 8 |
| 4 | 1004.13 | 532.07 | 522.31 | 523.52 | 525.12 | 524.69 | 524.85 |
| 5 | 1003.06 | 501.60 | 489.88 | 491.06 | 491.09 | 492.00 | 492.03 |
| 6 | 1003.18 | 493.02 | 481.56 | 481.79 | 482.27 | 482.62 | 482.85 |
| 7 | 1001.43 | 482.73 | 470.70 | 470.33 | 468.88 | 469.45 | 469.18 |
| 8 | 999.78 | 477.80 | 464.75 | 463.09 | 463.02 | 462.85 | 463.16 |
| 9 | 971.95 | 474.90 | 460.40 | 458.80 | 458.40 | 458.51 | 458.46 |
| 10 | 933.33 | 472.66 | 456.27 | 452.34 | 451.60 | 451.25 | 451.08 |

Comparing values between different *m* and the same degree (each row of Table 5.2), the mean *MSE* values are much higher for *m*=2. These results were expected and can be explained by the matching algorithm behaviour. When *m*=2 in the moving sequence, the number of images in moving sequence is always close to the number in the fixed sequence. For example, supposing that fixed sequence has 18 images and the moving sequence has 20 images, the number of possible matches when *m*=2 is:

$$C_{38}^{42} = \frac{42!}{(42-38)!38!} = 111.930.$$

Now assuming that *m*=3 (only in moving sequence) the number of total frames of moving sequence (*N*) is given by:

$$N = m \times 20 + m \Leftrightarrow N = 63.$$

Then, for *N* = 63 the number of possible global matches comes:

$$C_{38}^{63} = \frac{63!}{(63-38)!38!} = 2.4e^{+17}.$$

Hence if *m*>2 there is a huge increase in possibilities of global matches explaining the high difference between mean *MSE* values for *m*=2 and *m*=3.

Increasing *m* does not mean that mean *MSE* value decreases. Differences between mean *MSE* values are only significant ($p<0.05$) between m = 2 and 3 and *m* = 3 and 4 for all degrees. Additionally, the difference between the results for m = 4 and 5 is also significant ($p<0.001$) to the polynomial of 10$^{th}$ degree. This fact is very important because the smaller the *m* value, the faster the processing time. Using the previous example and considering the total number of images in fixed sequence as *M* and comparing *m* = 5 with m = 6, the results found are the ones presented in Table 5.3.

**Table 5.3 - Number of required MSE calculations when using two different *m* values (*m*=5 and *m*=6).**

| | m = 5 | m = 6 |
|---|---|---|
| Fixed sequence | $M = 18 \times 2 + 2 = 38$ | $M = 18 \times 2 + 2 = 38$ |
| Moving sequence | $N = 20 \times 5 + 5 = 105$ | $N = 20 \times 6 + 6 = 126$ |
| MSE calculations | $M \times N = 38 \times 105 = \mathbf{3990}$ | $M \times N = 38 \times 126 = \mathbf{4788}$ |

Using values of Table 5.3 as example, when using *m*=5 there are less 798 *MSE* calculations to do. In addition, there are also less 21 images interpolations. Thus, using *m* = 5 the mean *MSE* values of all used degrees are the ones depicted in Figure 5.2.

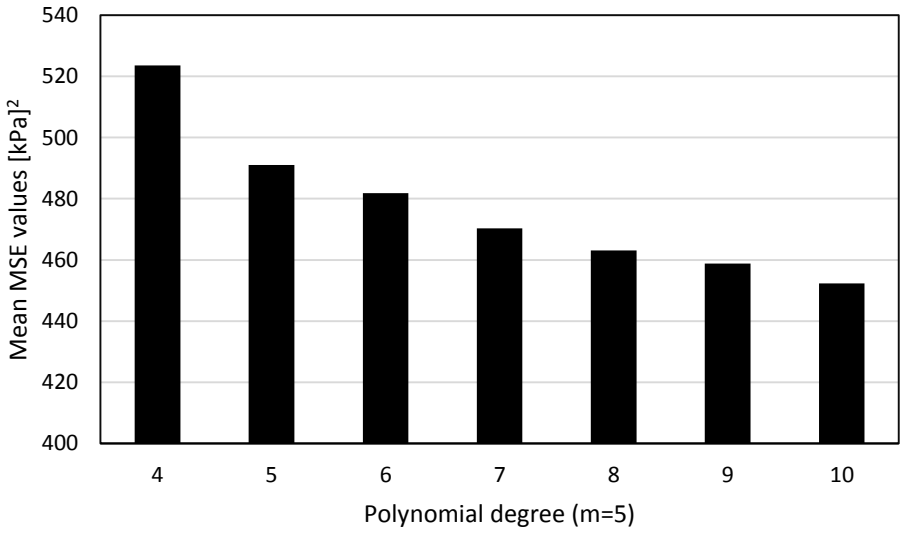


**Figure 5.2 - Plot of the mean MSE values calculated from the spatio-temporal alignment of real sequences of images. All used polynomial degrees are compared for *m*=5.**

The decreasing of mean MSE is very notorious when the polynomial degree is increased. Notice that all differences between mean MSE values are significant ($p$<0.05).

## 5.2.3 – RE assessment

Two temporal control deformations were applied to each sequence. Mean temporal and spatial errors were calculated after applying both control and obtained transformations to the original indexes. The temporal error was the mean of the differences between transformed indexes by both transformations (control and obtained). The procedure was the same to both linear and curved control deformations.

In order to compare different order polynomials accuracy, mean temporal error and mean spatial error were calculated for each polynomial degree and for different multiplication factors ($m$). Notice again that the fixed sequence has always $m$=2. Computational processing speed is also shown in Tables 5.6 and 5.9.

- **Linear deformation**

Concerning the mean spatial error (in case of linear deformation) the values are quite close for all degrees and for all $m$ values (Table 5.4). However, comparing values of mean temporal error between different $m$ values, it is observed that there is a significant difference ($p$<0.001) when $m$=2 and $m$≠2 (Table 5.5). This finding is explained by the poor matching achieved by the dynamic programing algorithm when both sequences have approximately the same number of frames. No significant differences were found between values obtained by the different degrees since the control deformation was linear and all polynomial degrees were greater than one. Thus, in presence of linear temporal deformations between different sequences, this framework has high accuracy both in time and space since all obtained error values were quite low.

As expected, the processing time increased with $m$ increasing. This fact is due the increasing in the number of needed calculations to match bigger sequences (with more images). There were no significant differences between processing speed of different degrees considering the same $m$ (each column of Table 5.6).

**Table 5.4 - Mean spatial error (in pixels) obtained after the spatio-temporal alignment of the deformed sequences. These values were computed using different polynomial degrees and different *m*.**

| | Multiplication factor (m) | | | | | | |
|---|---|---|---|---|---|---|---|
| Degree | 2 | 3 | 4 | 5 | 6 | 7 | 8 |
| 4 | 0.0144 | 0.0111 | 0.0096 | 0.0105 | 0.0090 | 0.0098 | 0.0102 |
| 5 | 0.0158 | 0.0169 | 0.0130 | 0.0146 | 0.0112 | 0.0144 | 0.0143 |
| 6 | 0.0170 | 0.0168 | 0.0125 | 0.0146 | 0.0112 | 0.0144 | 0.0139 |
| 7 | 0.0172 | 0.0171 | 0.0129 | 0.0150 | 0.0117 | 0.0148 | 0.0143 |
| 8 | 0.0168 | 0.0182 | 0.0141 | 0.0165 | 0.0127 | 0.0163 | 0.0158 |
| 9 | 0.0170 | 0.0181 | 0.0127 | 0.0165 | 0.0125 | 0.0164 | 0.0157 |
| 10 | 0.0188 | 0.0177 | 0.0124 | 0.0162 | 0.0123 | 0.0164 | 0.0151 |

**Table 5.5 - Mean temporal error (in frames) obtained after the spatio-temporal alignment of the deformed sequences. These values were computed using different polynomial degrees and different *m*.**

| | Multiplication factor (m) | | | | | | |
|---|---|---|---|---|---|---|---|
| Degree | 2 | 3 | 4 | 5 | 6 | 7 | 8 |
| 4 | 0.0923 | 0.0592 | 0.0528 | 0.0562 | 0.0531 | 0.0581 | 0.0521 |
| 5 | 0.0951 | 0.0612 | 0.0521 | 0.0555 | 0.0528 | 0.0594 | 0.0516 |
| 6 | 0.1047 | 0.0631 | 0.0545 | 0.0575 | 0.0566 | 0.0628 | 0.0539 |
| 7 | 0.1124 | 0.0652 | 0.0570 | 0.0612 | 0.0579 | 0.0646 | 0.0557 |
| 8 | 0.1157 | 0.0662 | 0.0607 | 0.0633 | 0.0597 | 0.0661 | 0.0572 |
| 9 | 0.1165 | 0.0677 | 0.0620 | 0.0647 | 0.0603 | 0.0666 | 0.0584 |
| 10 | 0.1191 | 0.0681 | 0.0637 | 0.0665 | 0.0605 | 0.0672 | 0.0590 |

**Table 5.6 - Mean computational processing time (in ms) obtained for all the performed spatio-temporal alignments. These values were computed using different polynomial degrees and different *m*. The computational speed was considered only to the temporal alignment algorithm.**

| | Multiplication factor (m) | | | | | | |
|---|---|---|---|---|---|---|---|
| Degree | 2 | 3 | 4 | 5 | 6 | 7 | 8 |
| 4 | 1420 | 948 | 1425 | 1691 | 2016 | 2673 | 3027 |
| 5 | 665 | 949 | 1413 | 1627 | 2037 | 2173 | 2895 |
| 6 | 601 | 1008 | 1452 | 1818 | 1938 | 2441 | 2672 |
| 7 | 755 | 1061 | 1364 | 1622 | 2109 | 2555 | 3155 |
| 8 | 736 | 1841 | 1414 | 1707 | 2127 | 2431 | 2908 |
| 9 | 640 | 965 | 1230 | 1662 | 1934 | 2389 | 2957 |
| 10 | 689 | 974 | 1300 | 1603 | 2108 | 2587 | 2848 |

- **Curved deformation**

In the case of the curved deformations, values of mean spatial error are quite similar excepting when $m$=2 ($p$<0.001) (Table 5.7). All values represent a high spatial alignment accuracy. When observing values of mean temporal error (Table 5.8), one detail is evident: when $m$=2 the mean temporal error is greater than 1 frame for all degrees. This high error is also explained by the matching algorithm behaviour, but adding the effect that when $m$=2 both sequences have approximately the same number of images resulting in an approximately linear relation established between images indexes by matching algorithm (since there are a few number of states – see $f_k(s)$ calculation in Chapter 4). As the control transformation is curved, the polynomial fails to fit the real transformation between both sequences. In addition, the same value of mean temporal error for all polynomial degrees when $m$=2 is explained by the same fact. Also the significant difference between mean spatial error when m=2 and m≠2 is explained by the high temporal error in sequence resampling.

Generally, for degrees greater than 5, the mean temporal errors decrease when increasing $m$ value. However this decrease is only significant ($p$<0.05) up to $m$=6.

Significant differences between mean temporal errors for different polynomial degrees were only found to the 4$^{th}$ degree ($p$<0.001) when $m$>4.

The processing time increased with $m$ increasing (Table 5.9). This fact is also due the increasing in the number of needed calculations to match bigger sequences (with more images).

**Table 5.7 - Mean spatial error (in pixels) obtained after the spatio-temporal alignment of the deformed sequences. These values were computed using different polynomial degrees and different *m*.**

| | Multiplication factor (m) | | | | | | |
|---|---|---|---|---|---|---|---|
| Degree | 2 | 3 | 4 | 5 | 6 | 7 | 8 |
| 4 | 0.0677 | 0.0183 | 0.0173 | 0.0182 | 0.0187 | 0.0186 | 0.0189 |
| 5 | 0.0677 | 0.0193 | 0.0159 | 0.0176 | 0.0211 | 0.0206 | 0.0228 |
| 6 | 0.0677 | 0.0228 | 0.0238 | 0.0267 | 0.0297 | 0.0297 | 0.0308 |
| 7 | 0.0677 | 0.0248 | 0.0273 | 0.0289 | 0.0308 | 0.0306 | 0.0314 |
| 8 | 0.0677 | 0.0231 | 0.0276 | 0.0285 | 0.0293 | 0.0285 | 0.0292 |
| 9 | 0.0677 | 0.0247 | 0.0351 | 0.0343 | 0.0347 | 0.0330 | 0.0337 |
| 10 | 0.0677 | 0.0280 | 0.0335 | 0.0322 | 0.0336 | 0.0326 | 0.0340 |

**Table 5.8 - Mean temporal error (in frames) obtained after the spatio-temporal alignment of the deformed sequences. These values were computed using different polynomial degrees and different *m*.**

| | Multiplication factor (m) | | | | | | |
|---|---|---|---|---|---|---|---|
| Degree | 2 | 3 | 4 | 5 | 6 | 7 | 8 |
| 4 | 1.7159 | 0.5432 | 0.2637 | 0.2148 | 0.2087 | 0.2081 | 0.2100 |
| 5 | 1.7159 | 0.5567 | 0.2321 | 0.1454 | 0.1202 | 0.1220 | 0.1210 |
| 6 | 1.7159 | 0.5461 | 0.2399 | 0.1511 | 0.1193 | 0.1217 | 0.1141 |
| 7 | 1.7159 | 0.5440 | 0.2461 | 0.1560 | 0.1217 | 0.1233 | 0.1163 |
| 8 | 1.7159 | 0.5396 | 0.2473 | 0.1549 | 0.1166 | 0.1182 | 0.1102 |
| 9 | 1.7159 | 0.5382 | 0.2455 | 0.1562 | 0.1158 | 0.1172 | 0.1081 |
| 10 | 1.7159 | 0.5404 | 0.2432 | 0.1522 | 0.1154 | 0.1151 | 0.1068 |

**Table 5.9 - Mean computational processing time (in ms) obtained for all the performed spatio-temporal alignments. These values were computed using different polynomial degrees and different *m*. The computational speed was considered only to the temporal alignment algorithm.**

| | Multiplication factor (m) | | | | | | |
|---|---|---|---|---|---|---|---|
| Degree | 2 | 3 | 4 | 5 | 6 | 7 | 8 |
| 4 | 681 | 980 | 1324 | 1656 | 2107 | 2851 | 3045 |
| 5 | 679 | 1092 | 2438 | 1756 | 2089 | 2677 | 3113 |
| 6 | 686 | 1001 | 1234 | 1524 | 1940 | 2724 | 3206 |
| 7 | 626 | 924 | 1446 | 1801 | 2234 | 2486 | 2960 |
| 8 | 638 | 1048 | 1383 | 1727 | 2186 | 2541 | 2945 |
| 9 | 700 | 1042 | 1337 | 1794 | 2162 | 3620 | 4154 |
| 10 | 715 | 1040 | 1400 | 1749 | 2254 | 2558 | 3158 |

The best mean temporal error obtained by the 4$^{th}$ degree polynomial in this work is better than the mean temporal error obtained by the same polynomial degree in Oliveira and Tavares (2012b). This fact is observable to both control deformations and is justified by the usage of the matching algorithm in this work which establishes a very good matching between images. In the referred work, the temporal pre-registration method is based in the establishment of a linear transformation between both sequences. However B-splines achieved better accuracy (except to the case where the distance between knots is equal to five) than the framework presented here. The main advantage of this framework is the low computational processing speed since it also achieves high accuracy

By last, the superior mean spatial errors in this work can be explained by the initial image interpolations when sequences are "expanded" by *m*. Nevertheless, high accuracy is also achieved since in most cases mean spatial error << 1 pixel.

The ability to fit the linear deformation by the 4th degree and 10th degree polynomials are compared in Figure 5.3. In the same figure are also shown the points found by the matching algorithm. The polynomials of other degrees are not represented because their curve are very similar and would damage legibility.

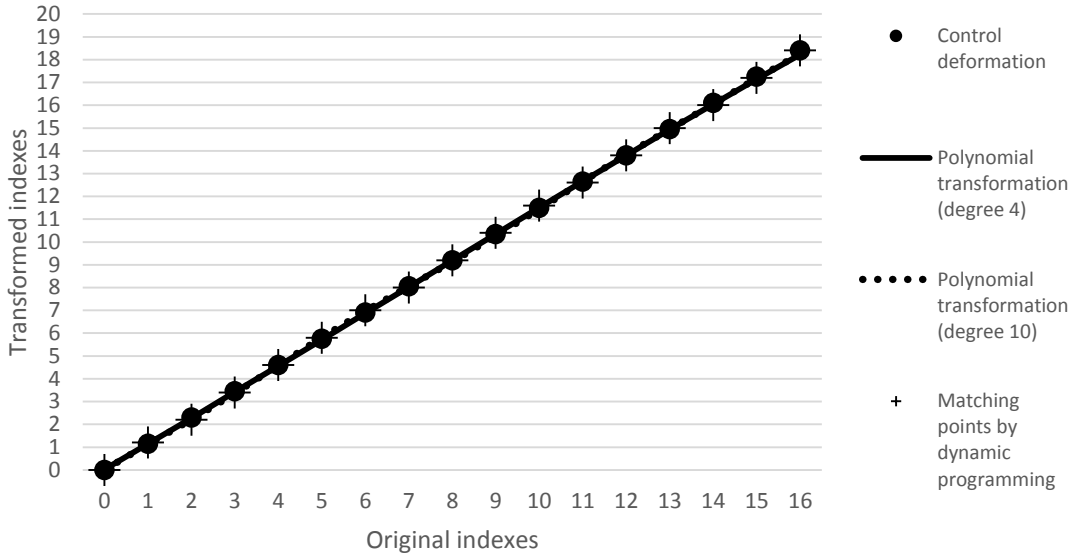


**Figure 5.3 – Comparison between two different polynomial transformation models (4th and 10th degree) when fitting points found by the dynamic programming algorithm. Indexes after the linear deformation are represented by circles.**

Matching algorithm found indexes very close to the transformed indexes (by the linear control deformation) as seen by the nearly perfect overlap in Figure 5.3. Moreover, both polynomial transformations fit similarly that points.

Concerning the curved control deformation, the same polynomial degrees are compared and also matching points are represented in Figure 5.4. The points found by the matching algorithm are also close to the deformed indexes but between the index 7 and 15 there is a slight deviation. This fact surely affects the polynomial accuracy. Even if the differences are almost indiscernible, it is possible to verify that the 10th degree polynomial fits better the matching points.

The spatio-temporal alignment is well demonstrated in Figure 5.5 where an original sequence is deformed by the curved deformation and then the spatio-temporal alignment framework re-aligns the sequences again. Beyond the orientation difference the temporal difference is very pronounced in several images. However, the spatio-temporal

alignment drives to good results nearly indistinguishable at human eye. The difference between aligned and original sequences is almost zero since the only non-zero pixels have very low intensities.

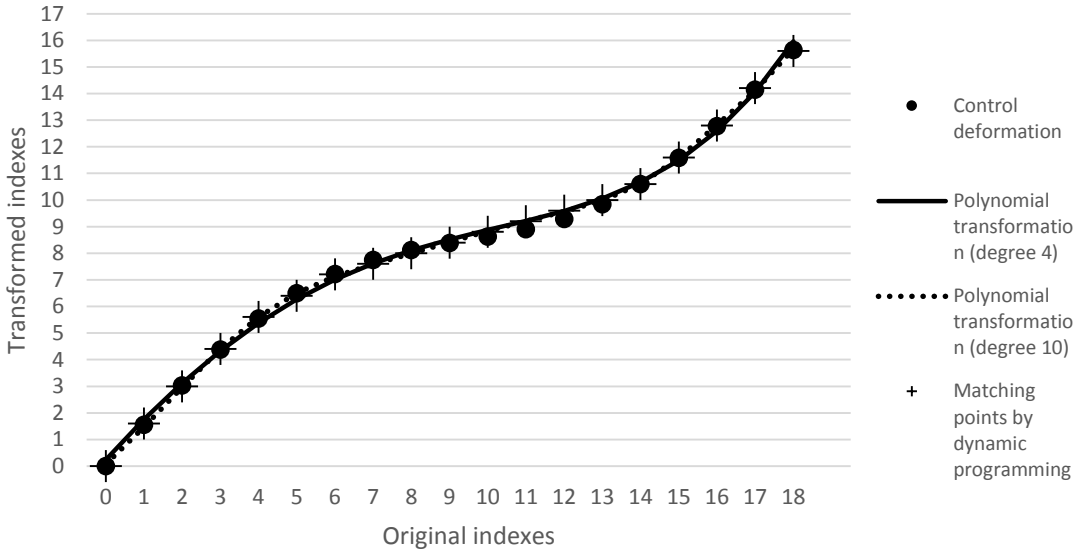


**Figure 5.4 - Comparison between two different polynomial transformation models (4th and 10th degree) when fitting points found by the dynamic programming algorithm. Indexes after the curved deformation are represented by circles.**

In Figure 5.5, the temporal delay of the moving (*M*) image sequence is very pronounced relatively to the fixed (*F*) image sequence. Moreover, the higher delay is seen between the 7th and the 15th degrees, approximately. Such higher delay corresponds to the range of smaller slope in the control deformation curve of Figure 5.4. Additionally, the delay imposed in the *M* sequence leads to an increase in the number of images.

In order to align *F* and *M* sequences, the spatio-temporal alignment framework starts with the spatial alignment. Thus, through the PA method, the rotation angle and translations between images are found. In this case, the rotation angle must be about -12˚ and translations approximately 0 pixels (according with the spatial control deformation applied). The values of the rigid geometrical transformation are then optimized. When the images of the moving sequence are spatially aligned, this sequence is expanded (using $m$ = 5) and the MSE is calculated between all images of both sequences (*F* sequence is always expanded using $m$=2). Then the matching of minimum global cost is established as seen in Figure 5.4 (matching indexes are represented by crosses). The coefficients of the polynomials are estimated by the least squares technique using the set of matching indexes. The aligned sequence is represented by $M_A$ in Figure 5.5.

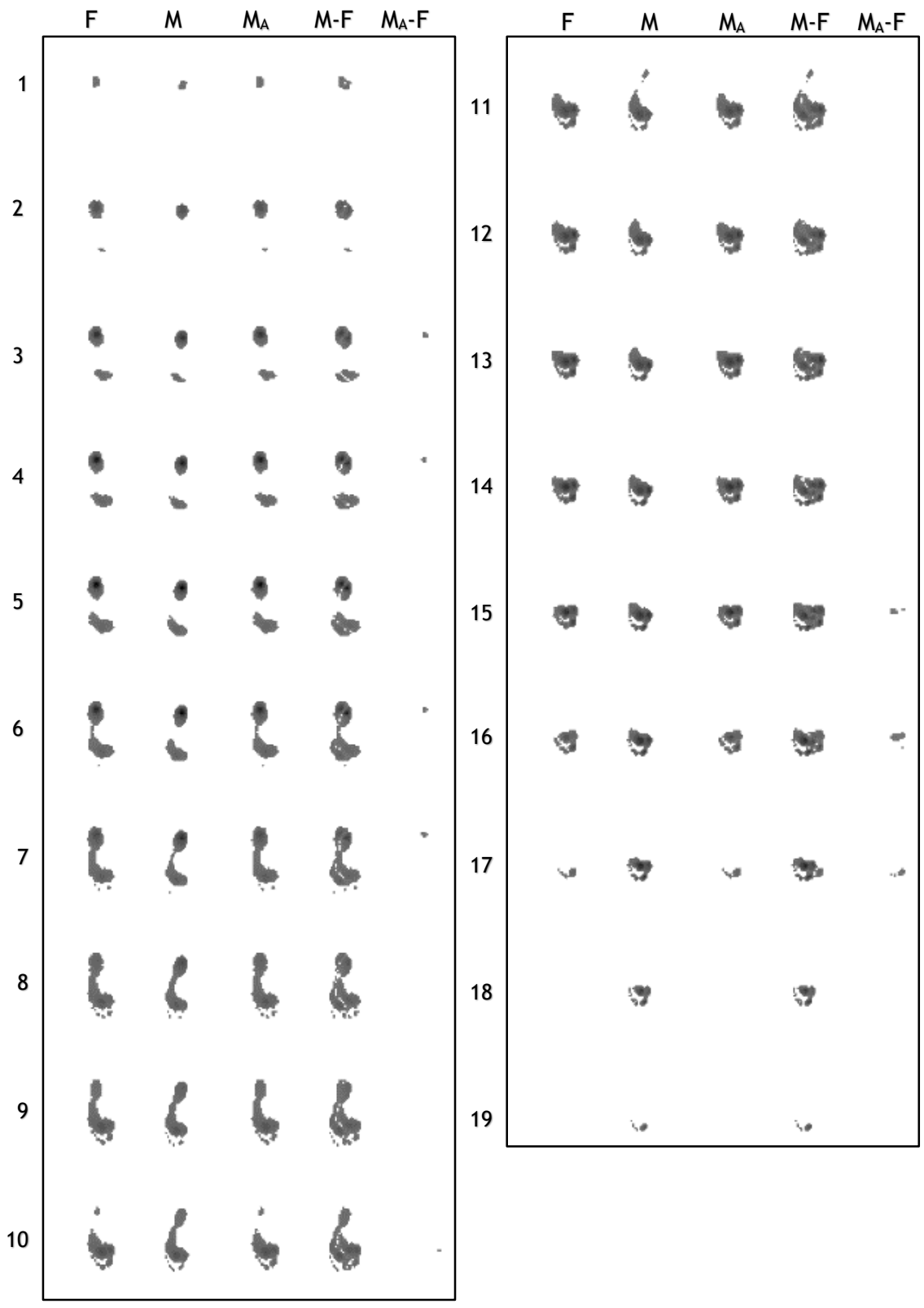


**Figure 5.5 – Representation of a full step. *F* is the original sequence, *M* is the deformed sequence, $M_A$ is the *M* sequence after the spatio-temporal alignment. *M-F* represents the difference between original and deformed sequences and $M_A$ – *F* represents the difference between the aligned and the original sequences.**

# 5.3 Plantar pressure parameters extraction

Plantar pressure values computed are shown in Tables 5.10-13. Image sequences from the two feet of 26 different subjects were used and analysed. To each parameter, its values were computed distinctly by *A – average of the values obtained individually from each original peak pressure image* - and *B – values computed directly from the peak pressure image obtained from a mean sequence (after spatio-alignment of the original sequences)*. At the end, the average and the standard deviation of those values calculated for all subjects were presented. Additionally, variables *A* and *B* are correlated by Pearson correlation coefficient and Intraclass correlation coefficient.

In Tables 5.10 and 5.11, the high correlation between *A* and *B* for the right foot is very evident. In fact, *PCC* values were very close to one for all parameters. The maximum pressure pixel relatively to the foot axis was the parameter with the smallest correlation between all parameters. However, such *PCC* value is still representative of high correlation between *A* and *B* as shown in Table 4.5.

All *ICC* values were also quite close to one and the lowest one was also registered to the maximum pressure pixel relatively to the foot axis. These findings confirmed the high consistency between both measuring methods.

Mean values and standard deviations were close between *A* and *B* to all parameters. As example considering mean values for *B*, the *COP* relatively to the foot axis had a medial displacement of -3.653 mm whereas *COP* relatively to the foot limit had a displacement of 130.7 mm. The maximum pressure pixel relatively to the foot axis was positioned 17.379 mm in the medial direction and relatively to the posterior limit there was a displacement of 184.8 mm. Mean *AI* value was 0.195 whereas *MAI* was 0.065. The high standard deviation errors were already expected since every subject has a personal gait and consequently parameters vary considerably between subjects.

As in the case of the right foot, there is also a strong correlation between *A* and *B* for the left foot. Thus, by Tables 5.12 and 5.13, it is very notorious that *PCC* values were very close to one for all parameters except for the maximum pressure pixel relatively to the foot limit. This parameter registered the smallest correlation between *A* and *B* (0.673); however, it is a good correlation yet. In addition, the other obtained *PCC* values were representative of high correlations between *A* and *B* as shown in Table 4.5.

All *ICC* values were representative of high consistency between methods *A* and *B* for the left foot. Again, there is an exception to the maximum pressure pixel relatively to the foot limit where the obtained *ICC* value represents a reasonable reliability.

**Table 5.10 – Right foot. Calculation of *PCC* and *ICC* between *A* and *B* to the *COP* parameters and to the maximum pressure pixel relatively to the foot axis.**

| | Right foot | | | | | |
|---|---|---|---|---|---|---|
| | COP relatively to foot axis (mm) | | COP relatively to foot limit (mm) | | Maximum pressure pixel relatively to the foot axis (mm) | |
| Subject | A | B | A | B | A | B |
| **1** | -3.102 | -3.928 | 139.8 | 144.3 | -5.198 | -4.337 |
| **2** | -3.089 | -2.236 | 134.3 | 134.2 | -20.363 | -26.756 |
| **3** | -0.287 | -0.883 | 133.8 | 131.5 | -4.075 | -4.201 |
| **4** | -0.667 | -0.151 | 123.9 | 119.8 | -3.440 | -0.202 |
| **5** | 0.093 | 0.452 | 132.8 | 134.4 | -1.901 | 0.000 |
| **6** | -0.846 | -1.540 | 118.6 | 116.9 | -2.378 | -2.620 |
| **7** | -4.762 | -5.578 | 140.4 | 139.6 | -28.647 | -7.874 |
| **8** | -0.687 | -1.771 | 129.3 | 130.6 | -40.175 | -43.274 |
| **9** | -0.048 | -0.345 | 133.2 | 134.7 | 6.194 | -6.253 |
| **10** | -4.070 | -2.679 | 132.6 | 133.9 | -43.148 | -40.658 |
| **11** | -6.184 | -7.442 | 132.1 | 129.7 | -21.700 | -38.157 |
| **12** | -3.903 | -4.229 | 149.4 | 152.3 | -14.816 | -4.869 |
| **13** | -5.767 | -6.301 | 130.4 | 129.0 | -31.906 | -32.086 |
| **14** | -8.381 | -9.485 | 126.4 | 125.2 | -28.903 | -28.380 |
| **15** | -4.838 | -3.931 | 136.5 | 133.3 | -18.388 | -8.609 |
| **16** | -3.410 | -3.156 | 136.3 | 135.9 | -35.936 | -38.019 |
| **17** | -10.397 | -10.859 | 143.2 | 139.5 | -49.785 | -52.310 |
| **18** | -4.825 | -4.582 | 132.6 | 133.8 | -32.700 | -34.681 |
| **19** | -5.269 | -5.888 | 126.8 | 130.8 | -33.820 | -36.306 |
| **20** | -2.492 | -3.333 | 124.9 | 126.3 | -7.006 | 8.805 |
| **21** | -1.839 | -1.308 | 118.2 | 118.0 | 5.163 | 5.704 |
| **22** | -3.141 | -3.941 | 112.0 | 108.3 | -3.612 | -8.598 |
| **23** | -3.426 | -2.981 | 123.4 | 122.9 | -22.194 | 0.000 |
| **24** | -3.729 | -3.176 | 125.7 | 127.8 | -35.220 | -34.516 |
| **25** | -3.717 | -3.598 | 136.0 | 136.3 | -19.598 | -20.259 |
| **26** | -0.554 | -2.115 | 126.0 | 127.9 | 9.351 | 6.603 |
| **Average** | -3.436 | -3.653 | 130.7 | 130.7 | -18.623 | -17.379 |
| **Standard deviation** | 2.558 | 2.720 | 8.210 | 9.039 | 16.679 | 18.389 |
| **Pearson correlation coefficient** | | 0.960 | | 0.967 | | 0.882 |
| **Intraclass correlation coefficient** | | 0.958 | | 0.963 | | 0.878 |

This reasonable reliability could be improved using more sequences of the same foot (> 3 ) in the calculations because using just 3 sequences, a high deviation in one of them could have a high impact in the final results.

**Table 5.11 - Right foot. Calculation of *PCC* and *ICC* between *A* and *B* to the maximum pressure pixel relatively to the foot axis and to AI and MAI.**

| | Right foot | | | | | |
|---|---|---|---|---|---|---|
| | Maximum pressure pixel relatively to the foot limit (mm) | | AI | | MAI | |
| Subject | A | B | A | B | A | B |
| **1** | 38.3 | 42.8 | 0.176 | 0.205 | 0.043 | 0.047 |
| **2** | 216.5 | 228.5 | 0.211 | 0.235 | 0.063 | 0.058 |
| **3** | 196.6 | 195.4 | 0.228 | 0.226 | 0.097 | 0.101 |
| **4** | 32.3 | 19.4 | 0.287 | 0.277 | 0.170 | 0.163 |
| **5** | 192.4 | 193.9 | 0.201 | 0.218 | 0.068 | 0.074 |
| **6** | 196.4 | 195.4 | 0.181 | 0.181 | 0.044 | 0.040 |
| **7** | 212.7 | 197.3 | 0.221 | 0.235 | 0.085 | 0.093 |
| **8** | 230.8 | 231.5 | 0.256 | 0.262 | 0.114 | 0.113 |
| **9** | 196.2 | 209.6 | 0.263 | 0.263 | 0.155 | 0.158 |
| **10** | 226.9 | 230.7 | 0.244 | 0.258 | 0.112 | 0.118 |
| **11** | 165.6 | 240.2 | 0.072 | 0.074 | 0.017 | 0.015 |
| **12** | 231.9 | 221.5 | 0.107 | 0.129 | 0.022 | 0.033 |
| **13** | 226.7 | 225.5 | 0.209 | 0.199 | 0.063 | 0.062 |
| **14** | 208.3 | 210.0 | 0.096 | 0.112 | 0.025 | 0.027 |
| **15** | 210.9 | 191.6 | 0.201 | 0.215 | 0.069 | 0.069 |
| **16** | 252.4 | 251.6 | 0.190 | 0.201 | 0.046 | 0.047 |
| **17** | 255.4 | 244.9 | 0.167 | 0.155 | 0.033 | 0.025 |
| **18** | 230.2 | 233.7 | 0.060 | 0.044 | 0.015 | 0.007 |
| **19** | 228.0 | 230.0 | 0.096 | 0.095 | 0.015 | 0.021 |
| **20** | 211.3 | 200.3 | 0.231 | 0.234 | 0.073 | 0.077 |
| **21** | 170.0 | 169.2 | 0.224 | 0.215 | 0.072 | 0.059 |
| **22** | 24.5 | 14.8 | 0.195 | 0.184 | 0.037 | 0.029 |
| **23** | 181.6 | 176.7 | 0.174 | 0.180 | 0.042 | 0.035 |
| **24** | 226.1 | 229.8 | 0.198 | 0.221 | 0.060 | 0.074 |
| **25** | 143.3 | 195.8 | 0.225 | 0.249 | 0.086 | 0.089 |
| **26** | 76.5 | 23.8 | 0.185 | 0.194 | 0.051 | 0.057 |
| **Average** | 183.9 | 184.8 | 0.188 | 0.195 | 0.065 | 0.065 |
| **Standard deviation** | 66.8 | 72.5 | 0.059 | 0.060 | 0.040 | 0.041 |
| **Pearson correlation coefficient** | | 0.951 | | 0.977 | | 0.987 |
| **Intraclass correlation coefficient** | | 0.948 | | 0.976 | | 0.987 |

Again, as in the right foot, the mean values and standard deviations were close between *A* and *B* to all parameters. As example, considering mean values for *B*, the COP

relatively to the foot axis had a medial displacement of -2.914 mm whereas COP relatively to the foot limit had a displacement of 131.5 mm.

**Table 5.12 - Left foot. Calculation of *PCC* and *ICC* between *A* and *B* to the *COP* parameters and to the maximum pressure pixel relatively to the foot axis.**

| | Left foot | | | | | |
|---|---|---|---|---|---|---|
| | COP relatively to foot axis (mm) | | COP relatively to foot limit (mm) | | Maximum pressure pixel relatively to the foot axis (mm) | |
| Subject | A | B | A | B | A | B |
| **1** | -3.095 | -3.425 | 140.8 | 140.1 | -10.547 | -2.235 |
| **2** | -2.967 | -4.074 | 133.4 | 136.3 | 1.460 | -0.253 |
| **3** | 0.925 | 0.592 | 126.6 | 127.6 | 6.824 | -6.028 |
| **4** | -0.406 | 0.796 | 125.6 | 130.2 | 2.665 | -4.697 |
| **5** | -1.215 | -1.477 | 133.9 | 133.8 | -10.550 | -2.067 |
| **6** | -0.542 | -1.107 | 123.1 | 121.0 | -5.937 | -3.663 |
| **7** | -3.719 | -1.767 | 139.3 | 141.6 | -20.698 | -8.215 |
| **8** | -5.691 | -4.134 | 133.4 | 134.7 | -39.315 | -33.293 |
| **9** | -3.142 | -2.815 | 138.3 | 133.1 | -8.323 | -9.156 |
| **10** | -4.215 | -4.175 | 132.4 | 131.0 | -38.120 | -37.938 |
| **11** | -5.190 | -5.461 | 135.5 | 136.7 | -11.612 | -6.615 |
| **12** | -5.916 | -5.711 | 145.5 | 143.2 | -32.815 | -34.180 |
| **13** | -2.519 | -0.596 | 119.2 | 119.5 | 2.501 | -2.092 |
| **14** | -6.662 | -6.320 | 125.8 | 124.8 | -28.504 | -26.583 |
| **15** | -2.467 | -2.959 | 144.9 | 145.3 | -8.356 | -9.026 |
| **16** | -1.209 | -1.234 | 127.3 | 129.4 | -12.641 | -31.213 |
| **17** | -5.814 | -5.356 | 146.6 | 147.6 | -19.632 | -9.054 |
| **18** | -4.669 | -4.346 | 138.8 | 139.2 | -16.840 | -30.172 |
| **19** | -2.092 | -3.228 | 120.4 | 119.8 | -6.779 | -10.290 |
| **20** | 1.960 | 0.751 | 117.3 | 119.1 | 2.876 | -0.352 |
| **21** | 0.964 | -0.498 | 115.5 | 118.7 | 4.485 | 1.894 |
| **22** | -2.098 | -1.914 | 128.9 | 130.2 | -6.438 | -5.752 |
| **23** | -2.524 | -3.654 | 118.6 | 117.8 | -0.774 | -5.828 |
| **24** | -5.050 | -6.497 | 132.9 | 132.7 | -36.336 | -35.843 |
| **25** | -3.133 | -3.793 | 134.5 | 134.1 | -5.330 | -9.017 |
| **26** | -3.521 | -3.371 | 128.2 | 130.9 | -18.991 | -30.213 |
| **Average** | -2.846 | -2.914 | 131.0 | 131.5 | -12.220 | -13.534 |
| **Standard deviation** | 2.261 | 2.138 | 8.902 | 8.638 | 13.685 | 13.333 |
| **Pearson correlation coefficient** | | 0.907 | | 0.974 | | 0.847 |
| **Intraclass correlation coefficient** | | 0.906 | | 0.973 | | 0.847 |

The maximum pressure pixel relatively to the foot axis was positioned -13.534 mm in the medial direction and relatively to the posterior limit there was a displacement of 176.5 mm.

**Table 5.13 - Left foot. Calculation of *PCC* and *ICC* between *A* and *B* to the maximum pressure pixel relatively to the foot axis and to AI and MAI.**

| | Left foot | | | | | |
|---|---|---|---|---|---|---|
| | Maximum pressure pixel relatively to the foot limit (mm) | | AI | | MAI | |
| Subject | A | B | A | B | A | B |
| **1** | 103.0 | 33.5 | 0.167 | 0.206 | 0.044 | 0.045 |
| **2** | 188.3 | 185.7 | 0.226 | 0.221 | 0.058 | 0.058 |
| **3** | 184.1 | 192.4 | 0.232 | 0.224 | 0.120 | 0.113 |
| **4** | 135.4 | 194.5 | 0.296 | 0.303 | 0.203 | 0.207 |
| **5** | 190.7 | 196.4 | 0.215 | 0.219 | 0.061 | 0.063 |
| **6** | 196.5 | 195.7 | 0.181 | 0.199 | 0.050 | 0.049 |
| **7** | 199.5 | 191.0 | 0.240 | 0.249 | 0.105 | 0.114 |
| **8** | 232.3 | 234.0 | 0.233 | 0.235 | 0.071 | 0.074 |
| **9** | 207.1 | 203.7 | 0.265 | 0.281 | 0.140 | 0.147 |
| **10** | 222.7 | 224.2 | 0.229 | 0.220 | 0.086 | 0.074 |
| **11** | 210.7 | 37.2 | 0.062 | 0.079 | 0.018 | 0.024 |
| **12** | 264.6 | 256.3 | 0.090 | 0.080 | 0.023 | 0.018 |
| **13** | 85.8 | 35.1 | 0.236 | 0.227 | 0.067 | 0.057 |
| **14** | 210.9 | 210.8 | 0.132 | 0.152 | 0.041 | 0.049 |
| **15** | 194.5 | 195.3 | 0.228 | 0.243 | 0.090 | 0.097 |
| **16** | 109.1 | 252.7 | 0.193 | 0.219 | 0.044 | 0.049 |
| **17** | 232.3 | 218.7 | 0.186 | 0.199 | 0.044 | 0.046 |
| **18** | 215.0 | 230.5 | 0.102 | 0.148 | 0.027 | 0.018 |
| **19** | 190.5 | 189.8 | 0.111 | 0.156 | 0.018 | 0.018 |
| **20** | 197.2 | 197.9 | 0.243 | 0.247 | 0.097 | 0.098 |
| **21** | 176.8 | 179.9 | 0.226 | 0.242 | 0.073 | 0.084 |
| **22** | 190.6 | 191.8 | 0.245 | 0.243 | 0.071 | 0.069 |
| **23** | 80.2 | 33.0 | 0.157 | 0.167 | 0.040 | 0.036 |
| **24** | 229.1 | 229.8 | 0.189 | 0.204 | 0.063 | 0.075 |
| **25** | 95.2 | 42.8 | 0.249 | 0.244 | 0.102 | 0.101 |
| **26** | 161.7 | 235.2 | 0.149 | 0.171 | 0.042 | 0.056 |
| **Average** | 180.9 | 176.5 | 0.195 | 0.207 | 0.069 | 0.071 |
| **Standard deviation** | 49.6 | 72.6 | 0.059 | 0.053 | 0.042 | 0.043 |
| **Pearson correlation coefficient** | | 0.673 | | 0.965 | | 0.987 |
| **Intraclass correlation coefficient** | | 0.627 | | 0.960 | | 0.987 |

Mean AI value was 0.207 whereas MAI was 0.071. There are high standard deviation errors due the reason previously pointed.

In conclusion, *PCC* and *ICC* showed that using a mean sequence of images could be a good solution to access parameters with relevance in plantar pressure studies. Such procedure can avoid time-consuming analysis of many sequences saving time and resources to the clinician and the clinic.

# 5.4 Summary

The MSE and RE results for the spatial alignment demonstrate that PA method has poor accuracy in spatial alignment of plantar pressure images. This fact is confirmed by the large difference in MSE values between the framework using the optimization procedure and the methods based only in PA. However, PA method shows high accuracy when images differ only by rotation and translation (rigid geometric transformation). In addition, it has low computational processing time. Notice that differences in accuracy are found using real intensities values or binary intensities of image pixels in PA methods.

The "expansion" of the number of images of both sequences can avoid polynomial instability and help (significantly) to improve accuracy. However it increases the computational processing speed. This accuracy increase is confirmed by the MSE values calculated. MSE values also confirm a significant accuracy increase when the polynomial degree is increased (up to the $10^{th}$ degree).

High accuracy is also verified through mean temporal and spatial errors between original image sequences and the aligned sequences previously deformed by both linear and curved deformations. An important vantage of the developed spatio-temporal alignment algorithm is the low processing time verified.

ICC and PCC were very close to one for all parameters used in this work excepting for the maximum pressure relatively to the foot limit. Nevertheless, the results indicate high correlation and consistency between the parameters obtained by both methods. Even in the case of the maximum pressure relatively to the foot limit there is a good correlation and a reasonable consistency.

Consequently, the framework proposed in this work can be a decisive tool, reducing the number of trials and maximizing the relevant information in plantar pressure analysis.

# Chapter 6 – Conclusions and future perspectives

Plantar pressure data provides crucial information about several pathologies and sports issues. This information is extracted from the plantar pressure patterns by means of parameters as the peak pressure pixel location, COP, AI and MAI. Image alignment is a valuable tool helping the researcher in the task of the relevant information search.

In this work, fast alternative solutions were proposed in order to achieve the spatio-temporal alignment of plantar pressure image sequences. Thus, PA based methods were used in the spatial alignment of plantar pressure images.

In the spatio-temporal alignment framework, the PA method was used as a pre-registration algorithm followed by an optimization procedure. After this spatial alignment, the framework used a dynamic programing based algorithm to match images from different sequences. Finally, a polynomial temporal relationship between both sequences is established. The accuracy of the framework was accessed through the MSE calculation between the aligned and the template real sequences. In addition, control deformations applied to all image sequences allowed to find mean temporal and spatial errors between original and aligned image sequences.

This work contributed to the development of the current spatio-temporal alignment algorithms found in literature.

The use of polynomials to describe the temporal relationship between images from different sequences is a fast solution and the high degree polynomials (up to $10^{th}$ degree) showed high accuracy. However, the central drawbacks of using polynomials are the instability of high degree polynomials and the strong dependence on the number of images in each sequence.

The dynamic programming algorithm is a good solution to establish the correspondence between images from different sequences. This approach would be an alternative method to use in other alignment problems involving temporal alignment.

The principal axes method can be a good solution to align similar images differing only by a rotation and displacements in *x* and *y* axes. Nevertheless, it is not an accurate method to align images with different shapes and data contents.

In this work, there were results pointing to the fact that the usage of a mean sequence can avoid time consuming analysis of several sequences to extract reliable relevant parameters.

In the sequence of the developed work, there are relevant possible future perspectives:

- To find correspondent reliable features between peak pressure images to calculate the centroids of the objects in order to increase accuracy of *PA* method.

- To change the parameter used to build the cost matrix. *MSE* is highly dependent of displacements and rotation between objects. It would be better to find a parameter invariant to translations and rotation. Thereby the temporal alignment would be done before the spatial alignment or even simultaneously.

- To use the matching algorithm to establish a pre-alignment in the framework of Oliveira and Tavares (2012). In this framework, B-splines would be used instead of polynomials and then a temporal optimization algorithm would be employed. This reformulation would reduce drastically the processing time of all framework.

- To test the use of mean image sequences built through the process described in this work in a real clinical environment.

# References

Ashburner, J. (2007). A fast diffeomorphic image registration algorithm. NeuroImage. 38: 95-113.

Bacarin, T. A., Sacco, I. C. N., Henning, E. M. (2009). Plantar pressure distribution patterns during gate in diabetic neuropathy patients with a history of foot ulcers. Clinics. 64(2): 113-120.

Bastos, L. F., Tavares, J. M. R. S. (2004). Improvement of modal matching image objects in dynamic pedobarography using optimization techniques. In F. J. Perales & B. A. Draper (Eds.), Articulated Motion and Deformable Objects - Lecture Notes in Computer Science. Volume 3179/2004 (pp. 39-50). Berlin / Heidelberg: Springer.

Besl, P. J., McKay, N. D. (1992). A method for registration of 3-D shapes. IEEE Trans Patt Anal Mach Intell. 14(2):239-256.

Cavanagh, P. R., Rodgers, M. M. (1987). The arch index: a useful measure from footprints. J Biomech. 20(5):547-551.

Chu, W. C., Lee, S. H., Chu, W., Wang T. J., Lee, M. C. (1995). The use of arch index to characterize arch height: a digital image processing approach. IEEE Trans Biomed Eng. 42(11): 1088-1093.

Crum W. R., Hartkens T., Hill D. L. G. (2004). Non-rigid image registration: theory and practice. Brit J Radiol. 77: S140-S153.

De Ridder, R., Willems, T., Roosen, P. (2012). Plantar pressure distribution during gait and running in subjects with chronic ankle instability. Journal of Foot and Ankle Research. 5(1):32.

Fitzpatrick, J., West, J., Maurer C. (1998). Predicting error in rigid-body, point-based registration. IEEE Transactions on Medical Imaging. 17:694-702.

Fitzpatrick, J. M., Hill, D. L. G., Maurer, C. R., Jr. (2000). “Image Registration”, Handbook of Medical Imaging, Volume 2: Medical Image Processing and Analysis, SPIE Press, M. Sonka and J.M. Fitzpatrick, eds., pp. 447-513.

Footscanusa.com. “Let technology run its course”. Available at <http://footscanusa.com/wp-content/uploads/2010/08/RSSC-catalogus-070108-A4-for-web.pdf.> Accessed on 22th of April, 2013.

Giacomozzi, C. (2011). "Potentialities and Criticalities of Plantar Pressure Measurements in the Study of Foot Biomechanics: Devices, Methodologies and Applications ". Biomechanics in Applications. V. Klika, InTech.

Goryachev, Y., Debbi, E. M., Haim, A., Rozen, N., Wolf, A. (2011). Foot center of pressure manipulation and gait therapy influence lower limb muscle activation in patients with osteoarthritis of the knee. J Electromyogr Kinesiol. 21(5): 704-711.

Gurney, J. K., Kersting, U. G., Rosenbaum D. (2008). Between-day reliability of repeated plantar pressure distribution measurements in a normal population. Gait Posture. 27(4): 706-709.

Hajnal, J. V., Hill, D., David J. Hawkes, D. J. (2001). Medical Image Registration. CRC Press.

Harrison, A. J., Hillard, P. J. (2000). A moment-based technique for the automatic spatial alignment of plantar pressure data. Proc Inst of Mech Eng H. 214(3): 257-264.

Hoh, C. K., Dahlbom, M., Harris, G., Choi, Y., Hawkins, R. A., Philps, M. E., Maddahi, J. (1993). Automated iterative three-dimensional registration of positron emission tomography images. J Nucl Med. 34(11): 2009-2018.

Hughes, J., Pratt, L., Linge, K., Clarke, P., Klenerman, L. (1991). The reliability of pressure measurements: the EMED F system. Clin Biomech. 6(1): 14-18.

Lehmann, T. M., Gönner, C., Spitzer, K. (1999). Survey: interpolation methods in medical image processing. IEEE Transactions on Medical Imaging. 18(11): 1049-1075.

Maintz, J. B. A. and Viergever, M. A. (1998). A survey of medical image registration. Med. Image Anal., vol. 2, pp. 1-36.

Maribo, T., Stengaard-Pedersen, K., Jensen, L. D., Andersen, N. T., Schiottz-Christensen, B. (2011). Postural balance in low back pain patients: Intra-session reliability of center of pressure on a portable force platform and of the one leg stand test. Gait Posture. 34(2): 213-217.

Mattes, D., Haynor, D. R., Vesselle, H., Lewellen, T. K., Eubank, W. (2003). PET-CT image registration in the chest using free-form deformations. IEEE Trans Med Imaging. 22(1): 120-128.

McLaughin, R. A., Hipwell, J., Hawkes, D. J., Noble, J. A., Byrne, J. V., Cox, T. (2002). A comparison of 2D-3D intensity-based registration and feature-based registration for neurointerventions. Lecture Notes in Computer Science. 2489: 517-524.

Morrison, K. E., Hudson, D. J., Davis, I. S., Richards, J. G., Royer, T. D., Dierks, T. A., Kaminski, T. W. (2010). Plantar pressure during running in subjects with chronic ankle instability. Foot Ankle Int. 31(11):994-1000.

Nakhaee, Z., Rahimi, A., Abaee, M. Rezasaltoni, A., Kalantari, K. K. (2008). The relationship between the height of the medial longitudinal arch (MLA) and the ankle and knee injuries in professional runners. Foot. 18(2): 84-90.

Novel.de. "The quality in-shoe dynamic pressure measuring system". Available at < http://novel.de/novelcontent/pedar>. Accessed on 22th of April, 2013.

Novelusa.com. "Accurate. Reliable. Unique". Available at < http://www.novelusa.com/index.php?fuseaction=systems.emed>. Acessed on 22th of April, 2013.

Oliveira, F. P. M., Tavares, J. M. R. S. (2008). Algorithm of dynamic programming for optimization of the global matching between two contours defined by ordered points. Comput Model Eng Sci. 31(1): 1-12.

Oliveira, F. P. M., Tavares, J. M. R. S., Pataky, T. C. (2009a). Rapid pedobarographic image registration based on contour curvature and optimization. J Biomech. 42(15): 2620-2623.

Oliveira, F. P. M., Tavares, J. M. R. S., Pataky, T. C. (2009b). A versatile matching algorithm based on dynamic programming with circular order preserving. VipIMAGE 2009 - II ECCOMAS Thematic Conference on Computational Vision and Medical Image Processing, Taylor and Francis. pp. 269-274.

Oliveira, F. P. M., Tavares, J. M. R. S., Pataky, T. C. (2010). Registration of pedobarographic image data in the frequency domain. Comput Methods Biomech Biomed Engin. 13(6): 731-740.

Oliveira, F. P. M., Tavares J. M. R. S. (2011). Novel framework for registration of pedobarographic image data. Med Biol Eng Comput. 49(3): 313-323.

Oliveira, F. P. M., Sousa, A., Santos, R., Tavares J. M. R. S. (2011b). Spatio-temporal alignment of pedobarographic image sequences. Med Biol Eng Comput. 49(7): 843-850.

Oliveira, F. P. M., Tavares J. M. R. S. (2012a). Medical image registration: a review. Comput Methods Biomech Biomed Engin. DOI:10.1080/10255842.2012.670855 (in press).

Oliveira, F. P. M., Tavares J. M. R. S. (2012b). Enhanced Spatio-Temporal Alignment of Plantar Pressure Image Sequences using B-splines. Med Biol Eng Comput. DOI: 10.1007/s11517-012-0988-3 (in press).

Oliveira, F. P. M., Tavares J. M. R. S. (2012c). Registration of plantar pressure images. Int J Numer Method Biomed Eng. 28(6-7): 589-603.

Oliveira, F. P. M, Sousa, A., Santos, R., Tavares, J. M. R. S. (2012d). Towards an Efficient and Robust Foot Classification from Pedobarographic Images. Comput Methods Biomech Biomed Engin. 15(11): 1181-1188.

Orlin, M. and McPoil, T. (2000).Plantar Pressure Assessment. Phys Ther. 80(4):399-499.

Pataky, T. C., Goulermas, J. Y., Crompton, R. H. (2008b). A comparison of seven methods of within-subjects rigid-body pedobarographic image registration. J Biomechanics. 41(14): 3085-3089.

Pinho, R. R., Tavares, J. M. R. S. (2004). Dynamic pedobarography transitional objects by Lagrange's equation with FEM, modal matching and optimization techniques. In A. C. Campilho & M. S. Kamel (Eds.), Image Analysis and Recognition - Lecture Notes in Computer Science. Volume 3212/2004 (pp. 92-99): Springer.

Press, W. H., Teukolsky, S. A., Vetterling, W. T., Flannery, B. P. (2007). Numerical recipes: the art of scientific computing. New York: Cambridge University Press.

Razak, A. H. A., Zayegh, A., Rezaul, K. B., Wahab, Y. (2012). Foot plantar pressure measurement system: a review. Sensors. 12: 9884-9912.

Ribeiro, A. P., Trombini-Souza, F., Tessutti, V. D., Lima, F. R., João, S. M., Sacco, I. C. (2011). The effects of plantar fasciitis and pain on plantar pressure distribution of recreational runners. Clin Biomech. 26(2):194-199.

Roerdink, M., Haart, M. D., Daffertshofer, A., Donker, S. F., Geurts, A. C., Beek, P. J. (2006). Dynamical structure of center-of-pressure trajectories in patients recovering from stroke. *Exp Brain Res*. 174(2): 256-269.

Rohr K., Stiehl, H. S., Sprengel, R, Buzug, T. M., Weese, J, Kuhn, M. H. (2001). Landmark-based elastic registration using approximating thin-plate splines. IEEE Trans Med Imaging. 20(6): 526-534.

Roy, H., Bhattacharya, K., Deb, S., Ray, K. (2012). Arch Index: an easier approach for arch height (a regression analysis). Al Ameen J Med Sci. 5(2): 137-146.

Rueckert, D., Sonoda, L.I., Hayes, C., Hill, D. L. G., Leach, M. O., Hawkes, D. J. (1999). Nonrigid registration using free-form deformations: application to breast MR images. IEEE Trans Med Imaging. 18(8):712-721.

Shen D. (2007). Image registration by local histogram matching. Patt Recogn. 40: 1161-1172.

Studholme, C., Hill, D. L. G., Hawkes, D. J. (1996). Automated 3-D registration of MR and CT images of the head. Med Imag Anal. 1(2): 163-175.

Studholme, C., Hill, D. L. G., Hawkes, D. J. (1999). An overlap invariante entropy measure of 3D medical image alignment. Patt Recogn. 32(1): 71-86.

Tábuas, C. (2012). Análise de pressão plantar para fins de diagnóstico. Master's Thesis. FEUP.

Tavares, J. M. R. S., Barbosa, J. M. G., Padilha, A. J. (2000). Matching image objects in dynamic pedobarography. RecPad, 11th Portuguese Conference on Pattern Recognition. Porto, Portugal.

Tekscan.com."F-Scan system in-shoe plantar pressure analysis" Available at < http://www.tekscan.com/medical/system-fscan1.html >. Accessed on 22th of April, 2013.

Thévenaz, P., Blu, T., Unser, M. (2000). Interpolation revisited. IEEE Trans Med Imaging. 19(7): 739-758.

Van Gheluwe, B., Dananberg, H. J., Hagman, F., Vanstaen, K. (2006). Effects of hallux limitus on plantar foot pressure and foot kinematics during walking. J Am Podiatr Med Assoc. 96(5):428-36.

Waldecker, U. (2012). Pedographic classification and ulcer detection in the diabetic foot. Foot Ankle Surg. 18(1): 42-49.

Xiong, S., Goonetilleke, R. S., Witana, C. P., Weerashinge, T. W., Au, E. Y. (2010). Foot arch characterization: a review, a new metric, and a comparison. J Am Podiatr Med Assoc. 100(1):14-24.

Zitová, B., Flusser, J. (2003). Image registration methods: a survey. Image Vis Comput. 21:977-1000.